

See discussions, stats, and author profiles for this publication at: <https://www.researchgate.net/publication/239290092>

Thermal Stability and Segregation Processes in Self-Assembled Size-Selected $\text{Au}_x \text{Fe}_{1-x}$ Nanoparticles Deposited on TiO_2 (110): Composition Effects

ARTICLE *in* THE JOURNAL OF PHYSICAL CHEMISTRY C · JANUARY 2009

Impact Factor: 4.77 · DOI: 10.1021/jp806570a

CITATIONS

27

READS

26

4 AUTHORS, INCLUDING:



Luis K Ono

Okinawa Institute of Science and Technology

61 PUBLICATIONS 1,361 CITATIONS

SEE PROFILE

Article

Thermal Stability and Segregation Processes in Self-Assembled Size-Selected AuFe Nanoparticles Deposited on TiO(110): Composition Effects

A. Naitabdi, L. K. Ono, F. Behafarid, and B. Roldan Cuenya

J. Phys. Chem. C, **2009**, 113 (4), 1433-1446 • Publication Date (Web): 06 January 2009

Downloaded from <http://pubs.acs.org> on January 27, 2009

More About This Article

Additional resources and features associated with this article are available within the HTML version:

- Supporting Information
- Access to high resolution figures
- Links to articles and content related to this article
- Copyright permission to reproduce figures and/or text from this article

[View the Full Text HTML](#)



ACS Publications

High quality. High impact.

The Journal of Physical Chemistry C is published by the American Chemical Society. 1155 Sixteenth Street N.W., Washington, DC 20036

Thermal Stability and Segregation Processes in Self-Assembled Size-Selected $\text{Au}_x\text{Fe}_{1-x}$ Nanoparticles Deposited on $\text{TiO}_2(110)$: Composition Effects

A. Naitabdi, L. K. Ono, F. Behafarid, and B. Roldan Cuenya*,†,‡

Department of Physics, Nanoscience and Technology Center, and Department of Civil, Environmental, and Construction Engineering, University of Central Florida, Orlando, Florida 32816

Received: July 24, 2008; Revised Manuscript Received: November 25, 2008

In-situ scanning tunneling microscopy (STM) and X-ray photoelectron spectroscopy (XPS) measurements have been performed to investigate the formation and thermal stability of mono- and bimetallic $\text{Au}_x\text{Fe}_{1-x}$ ($x = 1, 0.8, 0.5, 0.2, 0$) nanoparticles (NPs) supported on $\text{TiO}_2(110)$. Nearly hexagonal arrangements of size-selected Au, Fe, and Au–Fe NPs with well-defined interparticle distances have been achieved by diblock-copolymer encapsulation. Upon stepwise annealing from 300 to 1060 °C, a remarkable thermal stability of the Au–Fe NPs was observed, maintaining their original spatial arrangement on the TiO_2 surface up to 900 °C. A majority phase of a gold–iron alloy (solid solution) was achieved for our $\text{Au}_{0.5}\text{Fe}_{0.5}$ NPs in the temperature range of 700 °C - 800 °C, and for $\text{Au}_{0.2}\text{Fe}_{0.8}$ NPs at 800 °C, while a phase mixture of bcc Fe and Au–Fe alloy was observed for the $\text{Au}_{0.8}\text{Fe}_{0.2}$ system at 800 °C–900 °C. For all samples the segregation of Au atoms toward the NP surface was detected upon high temperature annealing (800 °C) in vacuum. Nearly complete Au desorption was observed by XPS at 900 °C for $\text{Au}_{0.2}\text{Fe}_{0.8}$ NPs, at 1000 °C for $\text{Au}_{0.5}\text{Fe}_{0.5}$ NPs, and at 1060 °C for $\text{Au}_{0.8}\text{Fe}_{0.2}$ NPs. The enhanced thermal stability of Au in the $\text{Au}_{0.8}\text{Fe}_{0.2}$ NPs is believed to be related to the formation of core(Fe)/shell(Au) structures. Furthermore, contrary to the case of pure Fe or Fe-rich NPs where nearly complete Fe desorption or Fe diffusion into TiO_2 was observed at 1000 °C, an Fe signal was detected at this temperature for the Au-rich samples ($\text{Au}_{0.8}\text{Fe}_{0.2}$ and $\text{Au}_{0.5}\text{Fe}_{0.5}$).

Introduction

The physical and chemical properties of bimetallic systems have been found to differ strongly from their corresponding monometallic analogues^{1,2} and have therefore been the subject of intensive theoretical and experimental research.^{3–5} In the field of heterogeneous catalysis, oxide-supported bimetallic nanoparticles (NPs) have shown remarkably high activity and selectivity. Several mechanisms are believed to be responsible for such enhanced catalytic performance, including the presence of lower barriers for specific chemical reactions⁶ and improved resistance against poisoning and subsequent deactivation.⁷ Combining two active metal catalysts in a single nanoparticle induces fundamental changes in their electronic properties which are relevant for the activation of many reactions.^{4,8} In particular, charge-transfer between the two metals in a bimetallic system can favorably change the binding energy of adsorbates.^{3,6,9,10} Additionally, the catalytic activity can be tuned by systematically changing the composition of the elemental constituents in the bimetallic NPs.¹¹ Among the binary nanoscale alloy systems, Au–Fe NPs have received less attention^{12–17} due to the immiscibility of Au and Fe in the bulk. However, this is an interesting material system for optical, magnetic, and biomedical applications including drug delivery.^{17–20} For example, density-functional theory (DFT) calculations by Sun et al.¹⁷ revealed that the magnetic moment of the Fe core in core(Fe)-shell(Au) nanoparticles is significantly higher than that of bulk Fe while the Fe–Fe coupling remained ferromagnetic, independent of the thickness of the Au shell. In addition, the Au-coated Fe

clusters were found to have an enhanced chemical stability against oxidation and coalescence, diminishing the probability of free radical and thromboses formation in the human body.¹⁷ Thus, in order to take advantage of the biocompatibility and surface functionalization possibilities that this bimetallic system presents, it is crucial to be able to understand the conditions under which stable core(Fe)-shell(Au) NP structures can be experimentally obtained. Furthermore, Au–Fe nanoparticles are also considered promising catalytic systems for industrially relevant processes such as Fischer–Tropsch reactions, methanol synthesis from syngas and high temperature CO oxidation. To date, the high catalytic activity of gold NPs deposited on iron oxide has been demonstrated for the oxidation of CO, C_3H_8 , and C_3H_6 ,^{21–24} as well as the liquid-phase oxidation of O-hydroxybenzyl alcohol,²⁵ and ethylacetate combustion over Au and Fe NPs in a SiO_2 matrix.²⁶ The reactivity of truly bimetallic Au–Fe NPs systems is still vastly unexplored, but is currently being evaluated by our group.

Extensive theoretical studies have been dedicated to the understanding of effects that govern the structure and composition of bimetallic NPs, including alloying,^{27–29} segregation,^{28,30–34} cluster size,^{35–37} melting temperature,^{38,39} and surface reconstruction.⁴⁰ In general, the segregation processes are explained in terms of the atomic size mismatch and the surface energy difference between the metallic constituents. In addition, attention has been paid to how the chemical environment of the bimetallic system can affect segregation phenomena.⁴¹ Further, under oxidizing conditions, the element with the highest affinity for oxygen was found to have the highest tendency to surface segregation.⁴¹ Although the melting of small metal NPs usually occurs at lower temperatures than their bulk counterparts, the formation of an alloy through the introduction of a secondary metal component can stabilize the NPs and increase their onset

* To whom correspondence should be addressed. E-mail: roldan@physics.ucf.edu.

† Nanoscience and Technology Center.

‡ Department of Civil, Environmental and Construction Engineering.

melting temperature above those of the individual constituents. Molecular dynamics (MD) simulations by Mottet et al.³⁸ showed a considerable upward shift in the melting temperature of icosahedral Ag clusters when Ni and Cu impurities were introduced. This effect was attributed to the release of stress in the core, induced by the presence of Ni and Cu, leading to a superior stability of the clusters against thermal effects. A similar effect will be discussed here for our $\text{Au}_{0.2}\text{Fe}_{0.2}$ NPs.

Relatively few systematic experimental studies are available on the composition and surface structure of bimetallic NPs.^{5,6,42–44} Yi et al.⁴² reported the formation of a stable Pd–Au alloy in the temperature range of 427–727 °C, with a Au-rich surface.⁴² By means of XPS and scanning tunneling spectroscopy (STS) measurements, our group has recently monitored the formation and thermal stability of Au–Fe alloys in $\text{Au}_{0.5}\text{Fe}_{0.5}$ NPs deposited on $\text{TiO}_2(110)$.⁵ Our STS measurements revealed that separated Au and Fe grains coexisted within an individual Au–Fe NP after annealing at 300 °C. An Au–Fe alloy is formed upon annealing at 700 °C, with the marked appearance of an iron $d_{3z^2-r^2}$ electronic surface state. Further annealing at 900 °C resulted in the disappearance of the Fe surface state and in a drastic decrease of the Fe XPS signal.⁵ The latter effects were attributed to the segregation of Au to the NP surface. In both examples, Au was the element with the lowest surface energy.

In the present work we have performed *ex-situ* atomic force microscopy (AFM), *in situ* (ultrahigh vacuum, UHV) STM and XPS measurements in order to investigate the morphological and chemical stability of self-assembled size-selected $\text{Au}_x\text{Fe}_{1-x}$ ($x = 1, 0.8, 0.5, 0.2, 0$) NPs supported on $\text{TiO}_2(110)$. Through the *in situ* study, insight will be gained into the onset of alloy formation as well as segregation and atomic desorption phenomena in $\text{Au}_x\text{Fe}_{1-x}$ NPs with different compositions. Comparisons will be made with similarly synthesized pure Au and pure Fe NPs of similar average size. The outcome of these studies is relevant for the catalysis scientific community, since a better understanding of the composition and stability of bimetallic NPs under industrial reaction conditions (high temperature) could shed light on the mechanisms of catalyst reactivity and deactivation.

Experimental Details

$\text{Au}_x\text{Fe}_{1-x}$ nanoparticles ($x = 1, 0.8, 0.5, 0.2, 0$) were prepared by reverse micelle encapsulation⁴⁵ using a commercial diblock copolymer, polystyrene-*block*-poly(2-vinylpyridine) [PS(81000)-P2VP(14200), Polymer Source, Inc.]. Two metal salts, $(\text{HAuCl}_4 \cdot 3\text{H}_2\text{O})$ and (FeCl_3) , were added simultaneously to the polymeric solution previously obtained by dissolving 50 mg of the PS-P2VP in 10 mL of toluene. Subsequently, the solution was stirred for 48 h leading to the complete encapsulation of the two metal salts in the micelles. Using this synthesis method, the size of the NPs can be tuned by changing the length of the diblock-copolymer core (P2VP) or the metal-salt/PVP concentration ratio, while the interparticle distance can be controlled by modifying the length of the PS tail. Here, the metal salt to P2VP weight ratio was 0.6. The two metal salts were added in molar weight proportions leading to the formation of nominal $\text{Au}_{0.8}\text{Fe}_{0.2}$, $\text{Au}_{0.5}\text{Fe}_{0.5}$, and $\text{Au}_{0.2}\text{Fe}_{0.8}$ NPs inside the micelles. Although changes in the individual Au/Fe concentration ratio of NPs within the same sample are possible, compositional analysis carried out by XPS on these samples after annealing at 300 °C revealed that Au/Fe concentrations averaged over a sample region of 3.5 mm² are in agreement with the nominal compositions targeted in our synthesis.

A self-assembled monolayer of NPs was obtained on the $\text{TiO}_2(110)$ substrate by dip-coating the single crystal into the

gold–iron polymeric solution at a speed of 1 $\mu\text{m}/\text{s}$. Prior to the ex-situ NP deposition, the rutile $\text{TiO}_2(110)$ substrates were cleaned in UHV by several cycles of Ar^+ sputtering at room temperature (1 keV, 5 μA) for 45 min and annealing at 900–1000 °C for 20 min. This procedure was repeated until adequate substrate conductivity was obtained and large (1 × 1)- TiO_2 terraces were observed by STM.⁴⁶

These samples were then introduced in a multichamber UHV system (SPECS, GmbH) equipped with standard surface preparation and characterization techniques. The removal of the encapsulating polymer was achieved by an *in situ* oxygen–plasma treatment (O_2 pressure = 4×10^{-5} mbar, 80 min). XPS measurements ($\text{Al K}\alpha$, 1486.6 eV) conducted after the latter treatment corroborated the complete disappearance of the polymeric C-1s signal (see Suppl. Figure 1, Supporting Information). Subsequently, the samples were annealed *in situ* by electron bombardment in 100 °C intervals from 300 to 700 °C for 20 min (per interval) and from 800 to 1000 °C for 10 min (per interval). After each thermal treatment, XPS spectra were acquired at room temperature. After the subtraction of a linear background, the XPS spectra were fitted using Gaussian–Lorentzian line shapes with a small asymmetry term (CASA XPS software). The Au-4f XPS data were fitted using two spin–orbit doublets ($4f_{7/2}$, $4f_{5/2}$) corresponding to metallic Au (84.6 eV, 88.3 eV) and Au^{3+} /Au–Fe alloy (86.9 eV, 90.6 eV). The above BE values are higher than those previously reported for bulk Au (84 eV, 87.7 eV).⁴⁷ The origin of this difference will be discussed in the XPS section below. The Fe-2p spectra were fitted using three doublets ($2p_{3/2}$, $2p_{1/2}$) corresponding to Fe^0 (706.9 eV, 720.0 eV), Fe^{3+} /Au–Fe alloy/ $\text{FeTiO}_{3+\delta}$ (709.8 eV, 723.4 eV), and the corresponding Fe oxide satellite peaks (720 eV, 734 eV).^{48–52}

STM images were also measured (Aarhus STM, SPECS GmbH) following several of the annealing treatments after sample cooling to a stabilized temperature of 15 °C (STM). An electrochemically etched W tip was used for the STM measurements. The tip was cleaned in UHV by Ar^+ sputtering before each STM session.

To conduct additional morphological analysis over larger sample areas via AFM, a second set of samples was prepared using the same nanoparticle solutions and an identical $\text{TiO}_2(110)$ substrate precleaned in UHV as described above.

Results

A. Morphological Characterization (AFM, STM). Figure 1 displays *ex-situ* AFM images of (a) Au, (b) Fe, and (c–f) $\text{Au}_{0.5}\text{Fe}_{0.5}$ NPs obtained after atomic oxygen exposure in UHV (a–c) and subsequent annealing of the $\text{Au}_{0.5}\text{Fe}_{0.5}$ NPs at 500 °C (d), 700 °C (e), and 900 °C (f). A homogeneous surface coverage over large sample regions is observed. The increased roughness of the air-exposed $\text{TiO}_2(110)$ substrate prevents us from obtaining accurate information of the NP size due to the difficulty of defining a common background for all NPs. Histograms of the AFM height distributions (not shown) obtained from Figure 1 provided the following values: 4.3 ± 1.4 nm (pure Au), 4.3 ± 1.3 nm (pure Fe), and 2.9 ± 1.3 nm ($\text{Au}_{0.5}\text{Fe}_{0.5}$) after O_2 –plasma treatment. The average AFM heights of the $\text{Au}_{0.5}\text{Fe}_{0.5}$ NPs after subsequent annealing are: 3.2 ± 1.3 nm at 500 °C, 4.1 ± 1.4 nm at 700 °C, and 2.5 ± 0.9 nm at 900 °C. The particles are arranged in a nearly hexagonal 2D pattern, as can be seen in the STM images of $\text{Au}_{0.5}\text{Fe}_{0.5}$ NPs (taken after annealing at 900 °C) and the corresponding spatial autocorrelation plots of Figure 2.

Figure 3a–e shows additional STM images (200×200 nm²) acquired on a sample with self-assembled $\text{Au}_{0.5}\text{Fe}_{0.5}$ NPs

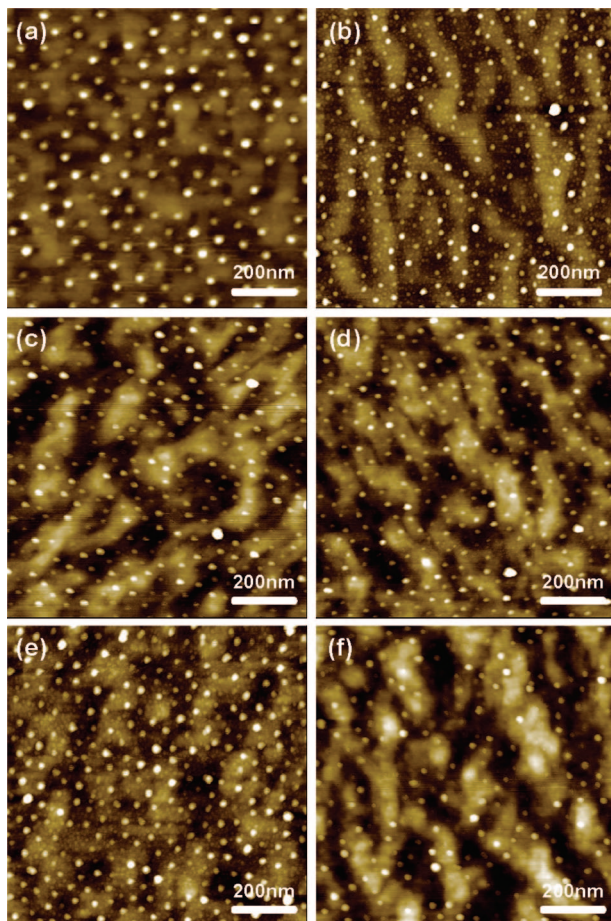


Figure 1. AFM images of (a) Au, (b) Fe, (c–f) Au_{0.5}Fe_{0.5} nanoparticles synthesized by inverse micelle encapsulation in PS(81000)-P2VP(142000) and supported on TiO₂(110). The images were taken in air after polymer removal in UHV by an O₂–plasma treatment (a–c) and subsequent annealing of the Au_{0.5}Fe_{0.5} NPs at 500 °C (d), 700 °C (e), and 900 °C (f).

deposited on TiO₂(110) after O₂ plasma treatment and subsequent annealing in UHV at (a) 300 °C, (b) 700 °C, (c) 800 °C, (d) 900 °C, and (e) 1000 °C. Figure 3f contains a high resolution ($50 \times 50 \text{ nm}^2$) image of a Au_{0.5}Fe_{0.5} NP on an atomically resolved TiO₂ terrace acquired after sample annealing at 1000 °C. Parallel atomic rows separated by a distance of 1.3 nm can be observed. This structure corresponds to the formation of the (1 × 2) reconstruction of the TiO₂(110) surface.^{53–55}

STM images of similarly prepared monometallic Au [Figure 3g,h] and Fe [Figure 3i] NPs were acquired after annealing at 300 °C (g), and 700 °C (h,i). Additional STM images of these two samples after annealing at 500 °C can be found in the Suppl. Figure 2. Our systematic AFM and STM studies indicate the stability of the spatial arrangement of the Au_{0.5}Fe_{0.5} and Au NPs up to 900 °C, and Fe NPs up to 700 °C, with an average interparticle distance d_{int} of $39 \pm 9 \text{ nm}$ (Au_{0.5}Fe_{0.5} at 900 °C, STM). The height (h) of the NPs also remains stable up to at least 800 °C. Representative histograms of the height (h) and interparticle distance (d_{int}) of Au_{0.5}Fe_{0.5}, Au, and Fe NPs obtained from the analysis of numerous STM images acquired after sample annealing at 900 °C (Au_{0.5}Fe_{0.5}) and 700 °C (Au and Fe) are shown in Figure 4. A summary of the measured average particle height (h) as a function of annealing temperature is shown in Figure 5. [The error bars correspond to the standard deviation calculated from the distribution of particle heights, Figure 4a, and interparticle distance, Figure 4b]. As an example,

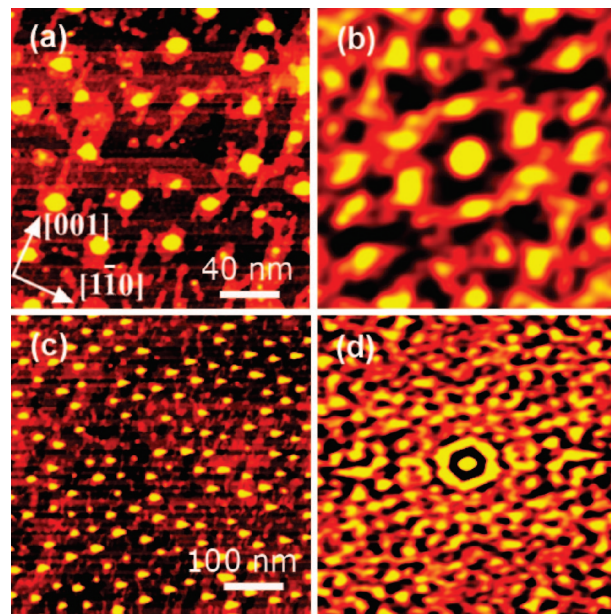


Figure 2. STM (a),(c) and corresponding spatial autocorrelation images (b),(d) of Au_{0.5}Fe_{0.5} nanoparticles synthesized by inverse micelle encapsulation and supported on TiO₂(110). The images were taken after sample annealing in UHV at 900 °C for 20 min.

for the Au_{0.5}Fe_{0.5} NPs only a moderate increase in the average NP height from $h = 4.6 \pm 1.4 \text{ nm}$ at 500 °C to $h = 5.7 \pm 1.3 \text{ nm}$ at 900 °C was observed, Figure 5. For higher annealing temperatures, a strong decrease in the Au_{0.5}Fe_{0.5} NP height was measured, with $h = 1.4 \pm 0.9 \text{ nm}$ at 1000 °C. The temperature of 900 °C appears to be a transition temperature, above which metal atoms start to desorb from the Au_{0.5}Fe_{0.5} NPs since a sharp reduction of both the NP height and its diameter (not shown) was measured. A similar trend was observed for the pure Au and pure Fe NPs, although the sharp decrease in the average height of Fe NPs occurred at an earlier temperature (between 700 and 900 °C). The NP height is considered here as the significant size parameter in our samples, since the NP diameter is obscured by tip convolution effects.

Annealing the Au_{0.5}Fe_{0.5} NPs at 1000 °C, Figure 3(e,f), resulted in the disappearance of the initial hexagonal NP arrangement, in Au and Fe atomic desorption, and in the development of a wider nanoparticle size distribution. At this temperature, wide terraces are observed in the TiO₂(110) surface. Only small variations in the roughness of the TiO₂ substrate (due to the initial O₂–plasma treatment) were noticed up to an annealing temperature of 700 °C. At this stage, no clear crystalline orientation can be observed on the substrate, but pearl-like TiO₂ structures (clusters) are present at the surface.⁵⁶ According to Stone et al.,⁵⁶ such morphologies are due to the diffusion of Ti^{δ+} interstitials from the bulk. Upon further annealing above 900 °C, the original TiO₂ clusters break up and atomic diffusion leads to the formation of parallel Ti and O rows along the [001] direction, Figure 3f. In these samples, the average rms roughness of the TiO₂ substrate obtained from the analysis of STM images acquired after the different thermal treatments is: $0.30 \pm 0.05 \text{ nm}$ after annealing at 300 °C, $0.31 \pm 0.06 \text{ nm}$ at 700 °C, $0.20 \pm 0.05 \text{ nm}$ at 800 °C, $0.16 \pm 0.03 \text{ nm}$ at 900 °C, and $0.07 \pm 0.03 \text{ nm}$ at 1000 °C (See Suppl. Figure 3, Supporting Information).

B. Electronic and Chemical Characterization (XPS).
1. Pure Au and Pure Fe Nanoparticles. Figure 6 displays XPS spectra from the Au-4f and Fe-2p core levels of two samples containing pure gold (Figure 6a) and pure Fe (Figure 6b) NPs

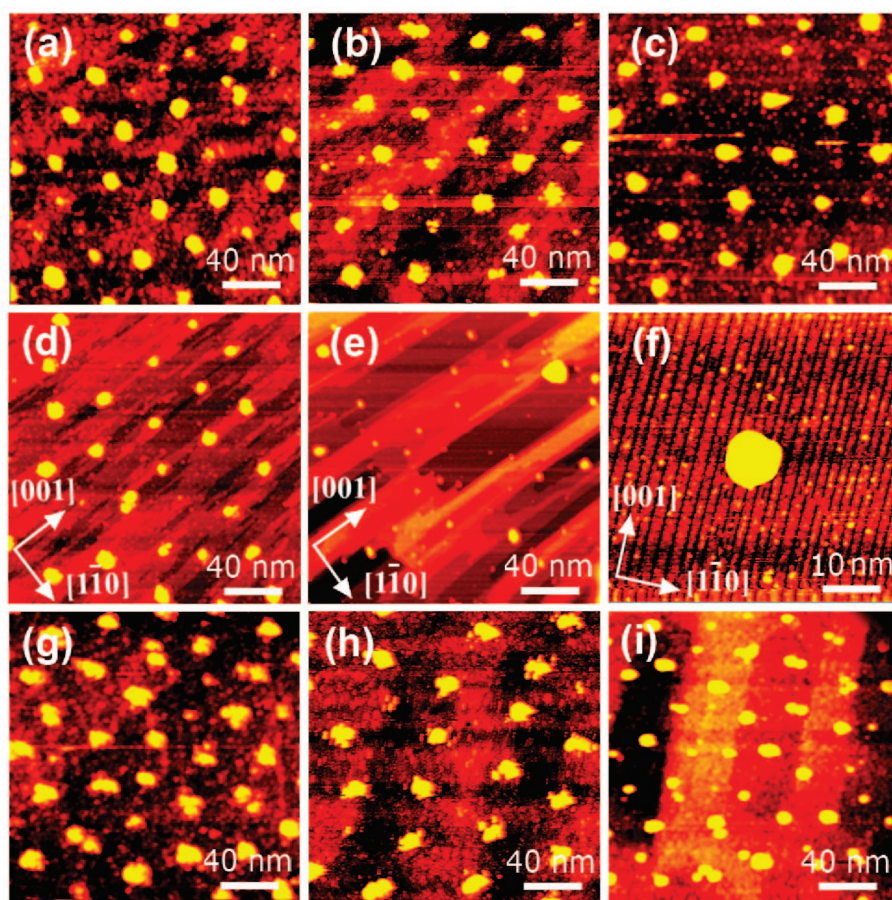


Figure 3. STM images of bimetallic $\text{Au}_{0.5}\text{Fe}_{0.5}$ (a–f), pure Au (g,h) and pure Fe (i) nanoparticles supported on $\text{TiO}_2(110)$ and measured at 15 °C after an *in situ* O_2 plasma treatment and subsequent annealing at: (a,g) 300 °C, (b,i) 700 °C, (c) 800 °C, (d,h) 900 °C, and (e,f) 1000 °C. With the exception of image (f) ($50 \times 50 \text{ nm}^2$), the rest of the images correspond to a scan region of ($200 \times 200 \text{ nm}^2$).

deposited on $\text{TiO}_2(110)$. The XPS data were acquired after an O_2 –plasma treatment and subsequent annealing from 300 to 1000 °C. Nanoparticle exposure to atomic oxygen resulted in the partial oxidation of Au, with 72% of the signal being Au^{3+} (binding energy BE = 87.1 eV of $\text{Au-4f}_{7/2}$) and 28% metallic Au.^{57,58} Figure 6a and Table 1. Interestingly, a large positive BE shift is observed in the Au-4f peaks of all our samples directly after atomic oxygen exposure (+1.1 eV with respect to Au^{3+}).^{59–61} After reduction of the Au^{3+} present below 300 °C, no changes in the binding energy of Au are observed in the temperature range from 300 to 600 °C,^{62,63} with a stable BE value of ~84.8 eV, Figure 6a. This value is +0.8 eV higher than the value of bulk metallic gold (84.0 eV, $\text{Au } 4\text{f}_{7/2}$). However, upon annealing at 700 °C, an additional shift of +0.5 eV (BE = 85.3 eV) is observed. As will be described in more detail in the discussion section, such shifts may be attributed to size-dependent final state effects,^{45,47,64} as well as to NP/support interactions.^{65–67} Since at 700 °C the NP size did not experience significant changes (Figure 5), Au–Ti interactions are believed to be responsible for the additional shift.^{47,65} A clear decrease in the Au signal is observed upon annealing at 900 °C, and no gold is detected by XPS after annealing at 1000 °C.

Figure 6b indicates that the pure Fe NPs are oxidized to Fe_2O_3 (711.6 eV, $\text{Fe-2p}_{3/2}$ in Fe_2O_3)⁴⁸ during the *in situ* O_2 –plasma treatment used to remove the encapsulating polymer, and that Fe^{3+} is stable at least up to 300 °C (100% signal, Table 1). Annealing at 500 °C resulted in partial reduction of Fe_2O_3 species to metallic Fe ($\text{Fe}^0\text{-2p}_{3/2}$ peak at 707.6 eV, 2%). In analogy to the case of the Au/TiO₂ system, the positive BE shifts (+0.7 eV with respect to bulk Fe^0 at 707.1 eV)^{48,49} observed

for our Fe/ TiO_2 NPs above 500 °C are attributed to final state effects^{45,64} in the photoemission process and to cluster/support interactions.^{66,67} In the temperature range of 500–900 °C the content of metallic Fe in these clusters increases, reaching a maximum of ~45% at 700–800 °C (Table 1). In addition, a shoulder is observed in the Fe-2p spectrum at ~710.5 eV [marked with an arrow in Figure 6b, 800 °C], indicating the presence of FeO_x ($\text{Fe}^{2+}\text{-2p}_{3/2}$ at ~709.6 eV)^{48–50} and/or $\text{FeTiO}_{3+\delta}$ compounds.^{51,52} Further details on this assignment are given in the discussion section.

2. $\text{Au}_{0.8}\text{Fe}_{0.2}$ Nanoparticles. The formation and thermal stability of Au–Fe alloys in size-selected NPs with different alloy compositions has been investigated *in situ* by XPS. Figure 7 shows thermally induced changes in the Au-4f (a) and Fe-2p (b) core levels of $\text{Au}_{0.8}\text{Fe}_{0.2}$ NPs supported on $\text{TiO}_2(110)$ after an O_2 plasma treatment followed by a stepwise annealing from 300 to 1000 °C. In Figure 7a, a BE shift of +0.5 eV with respect to bulk Au was measured after annealing at 300 °C, and an additional shift of +0.2 eV after annealing at 500 °C (BE = 84.7 eV, $\text{Au } 4\text{f}_{7/2}$). Above this temperature, the BE of Au is stable up to 1000 °C. Unlike the case of the pure Au NPs (lack of Au signal at 1000 °C), total desorption of Au from the $\text{Au}_{0.8}\text{Fe}_{0.2}$ NPs was not detected until the annealing temperature reached 1060 °C (not shown).

Another clear difference in the Au-4f XPS spectra of the Au-rich $\text{Au}_{0.8}\text{Fe}_{0.2}$ NPs [Figure 7a] with respect to their monometallic counterparts is the need to include an additional, weak high-BE component ($\text{Au-4f}_{7/2}$, 86.2–87 eV, ~10–14% of the total Au spectral area) in order to properly reproduce the raw

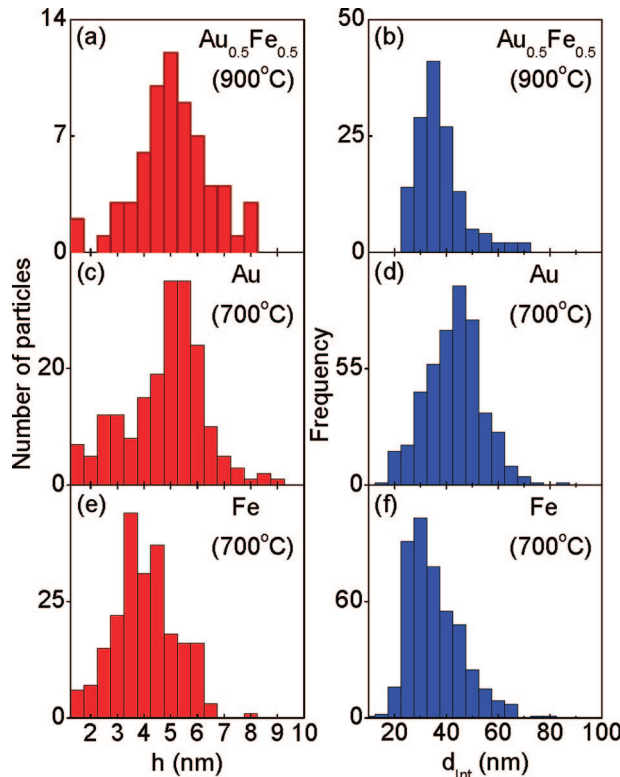


Figure 4. Representative histograms of the size and interparticle distance of Au_{0.5}Fe_{0.5} (a,b), Au (c,d), and Fe (e,f) NPs synthesized by inverse micelle encapsulation with PS(81000)-PVP(14200) and deposited on TiO₂(110). The data were extracted from a series of STM images acquired after polymer removal by an *in situ* atomic oxygen treatment and subsequent annealing in UHV at 900 °C (a,b) and 700 °C (c–f).

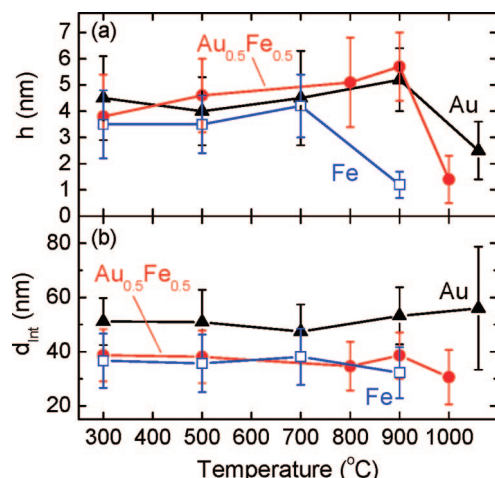


Figure 5. Evolution of the (a) average height (h) and (b) interparticle distance (d_{int}) of Au_{0.5}Fe_{0.5} (●), Au (▲) and Fe (□) nanoparticles with annealing temperature. The error bars given correspond to the standard deviation calculated from the distribution of particle heights and interparticle distances: shown in Figure 4.

data [see arrow in Figure 7a]. This component is attributed to Au–Fe bonding.^{68–71}

Figure 7b displays the evolution of the Fe-2p signal in Au_{0.8}Fe_{0.2} NPs with increasing annealing temperature. Similarly to the case of the pure Fe clusters, the O₂–plasma treatment employed leads to the oxidation of Fe (Fe³⁺, 712.6 eV). At 300 °C a small shift to lower BE (710.6 eV) is observed. However, in contrast to the case of the pure Fe clusters, where ~38% metallic Fe was detected at 500 °C (Table 1), two clear XPS

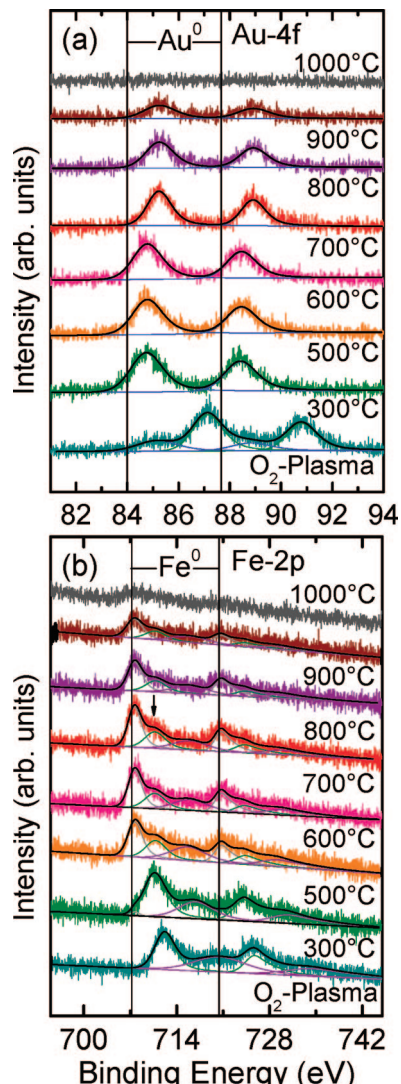


Figure 6. XPS spectra of (a) the Au-4f and (b) Fe-2p core level regions of pure Au (a) and pure Fe (b) nanoparticles supported on TiO₂(110). The spectra were acquired after O₂-plasma treatment and after subsequent *in situ* annealing from 300 to 700 °C for 20 min and from 800 to 1000 °C for 10 min. The reference straight solid lines indicate the binding energies of bulk Au and Fe. The arrow in (b) at a BE of 710.5 eV indicates the presence of oxidized Fe species (Fe²⁺/Fe³⁺) and/or an FeTiO_{3+δ} compound at the Fe/TiO₂ interface after annealing at 700 °C. The corresponding spectral least-squares fits for the different Au and Fe species are also shown, (solid lines).

peaks can be observed on the Au_{0.8}Fe_{0.2} NPs at 500 °C. The low energy peak (707.7 eV) corresponds to Fe⁰, while the high energy peak (710.6 eV) can be attributed to residual Fe–oxides and/or to the formation of a partial Au–Fe alloy. In order to test whether the latter component is exclusively related to the formation of a Au–Fe alloy or also, at least partially, to the presence of unreduced Fe-oxide compounds, similarly oxidized Au_{0.5}Fe_{0.5} NPs were exposed to a hot H₂–plasma treatment. The results of these experiments will be discussed below in the section dedicated to the Au_{0.5}Fe_{0.5} sample.

With increasing annealing temperature from 500 to 700 °C, the intensity of the second Fe component (710.6 eV) is reduced, which is attributed to the reduction of Fe oxide compounds. At 700 °C, ~35% of the Fe content is in the metallic state (707.6 eV, Table 1). Interestingly, further annealing to 800–900 °C leads to an increase in the 710.6 eV/707.6 eV intensity ratio [(Fe-oxide/Fe–Au alloy)/(Fe metal)]. Since at 800 °C Fe is

TABLE 1: Relative Content of the Different Au and Fe Phases of Pure Au, Pure Fe, $\text{Au}_{0.8}\text{Fe}_{0.2}$, $\text{Au}_{0.5}\text{Fe}_{0.5}$, and $\text{Au}_{0.2}\text{Fe}_{0.8}$ Nanoparticles Deposited on $\text{TiO}_2(110)$ Obtained from the Analysis of the Au-4f and Fe-2p XPS Data Shown in Figure 6, 7, 8, and 10^a

sample	temperature	phase content ($\pm 5\%$)				
		Au ⁰ 84.6–86.0 eV	Au ³⁺ 86.9–87.3 eV	Au–Fe Alloy 86.2–88.6 eV	Fe ⁰ 706.9–707.7 eV	Fe ³⁺ /Au–Fe Alloy/ $\text{FeTiO}_{3+\delta}$ 709.8–712.2 eV
Au-NPs	O ₂ –Plasma	28	72	—	—	—
	300 °C	100	0	—	—	—
	500 °C	100	0	—	—	—
	600 °C	100	0	—	—	—
	700 °C	100	0	—	—	—
	800 °C	100	0	—	—	—
	900 °C	100	0	—	—	—
	1000 °C	—	—	—	—	—
	O ₂ –Plasma	—	—	—	0	100
	300 °C	—	—	—	2	98
Fe-NPs	500 °C	—	—	—	38	62
	600 °C	—	—	—	43	57
	700 °C	—	—	—	45	55
	800 °C	—	—	—	46	54
	900 °C	—	—	—	44	56
	1000 °C	—	—	—	38	62
	O ₂ –Plasma	38	62	—	0	100
	300 °C	87	—	13	5	95
	500 °C	87	—	13	26	74
	600 °C	89	—	11	36	64
$\text{Au}_{0.8}\text{Fe}_{0.2}$ NPs	700 °C	90	—	10	35	65
	800 °C	88	—	12	30	70
	900 °C	86	—	14	19	81
	1000 °C	87	—	13	15	85
	O ₂ –Plasma	9	91	—	0	100
	300 °C	85	—	15	0	100
	500 °C	87	—	13	28	72
	600 °C	88	—	12	30	70
	700 °C	88	—	12	3	97
	800 °C	87	—	13	5	95
$\text{Au}_{0.5}\text{Fe}_{0.5}$ NPs	900 °C	73	—	27	11	89
	1000 °C	—	—	—	24	76
	O ₂ –Plasma	34	66	—	0	100
	300 °C	84	—	16	28	72
	500 °C	80	—	20	42	58
	600 °C	79	—	21	43	57
	700 °C	77	—	23	33	67
	800 °C	70	—	30	7	93
	900 °C	72	—	28	7	93
	1000 °C	—	—	—	—	—

^a The binding energies corresponding to the Au-4f_{7/2} and Fe-2p_{3/2} XPS peaks detected in each sample are indicated below each phase assignment in the top row.

expected to be completely reduced⁷² (with exception of the interfacial Fe atoms in contact with the oxide support), the sudden increase of the 710.6 eV component (see arrow in Figure 7b) signalized the formation of a partial Au–Fe alloy. At 900 °C only 19% of the remaining Fe in these NPs is in its pure metallic state, while the rest has formed an alloy with Au. In addition, a decrease in the total Fe signal is observed (by ~30% at 900 °C and by ~60% at 1000 °C) with respect to the value at RT, and incomplete desorption (Figure 7b) is noticed at 1000 °C. Due to the enhanced surface sensitivity of XPS, the marked decrease in the Fe signal above 700 °C (Figure 7b) might be attributed to the segregation of Au to the NP surface.

3. $\text{Au}_{0.5}\text{Fe}_{0.5}$ Nanoparticles. Figure 8 shows XPS spectra from the Au-4f (a) and Fe-2p (b) core levels of $\text{Au}_{0.5}\text{Fe}_{0.5}$ NPs acquired after O₂– plasma treatment and subsequent annealing at the indicated temperatures. In analogy to the case of the pure or Au-rich ($\text{Au}_{0.8}\text{Fe}_{0.2}$) NPs, a binding energy of 84.8 eV was measured for Au-4f_{7/2} after annealing at 300 °C, Figure 8a. Similar to the case of the Au-rich nanoparticles, for this new NP composition the Fe atoms still show a BE energy signifi-

cantly higher than that of bulk Fe (710.4 eV versus 707.1 eV for bulk Fe⁰) after annealing at 300 °C, suggesting the presence of oxidized Fe compounds, Figure 8b. The Au signal remained nearly stable up to an annealing temperature of 600 °C, where an additional positive BE shift was measured (+0.4 eV with respect to the 500 °C Au spectrum in $\text{Au}_{0.5}\text{Fe}_{0.5}$ NPs), Figure 8a. Analogously to the case of the Au-rich NPs, in the temperature range of 500 to 600 °C the two peaks observed in the Fe-2p spectra are attributed to Fe-oxides or a Au–Fe alloy (~710.4 eV), and to Fe⁰ (~707.7 eV) from the partial reduction of Fe_2O_3 , Figure 8b. Since both the Au-4f and the Fe-2p (710.4 eV) peaks in the $\text{Au}_{0.5}\text{Fe}_{0.5}$ NPs are shifted to higher BEs with respect to their pure NP counterparts at 600 °C, the onset of partial Au–Fe alloying at this temperature is plausible as will be discussed in detail below.

To separate the relative contributions from Fe–oxide and Au–Fe alloy (similar in BE) to the Fe-XPS spectra measured below 700 °C, we have performed *in situ* hot H₂–plasma treatments on a similarly prepared $\text{Au}_{0.5}\text{Fe}_{0.5}$ NP sample, Figure 9. A H₂ plasma treatment has been successfully used by Wang

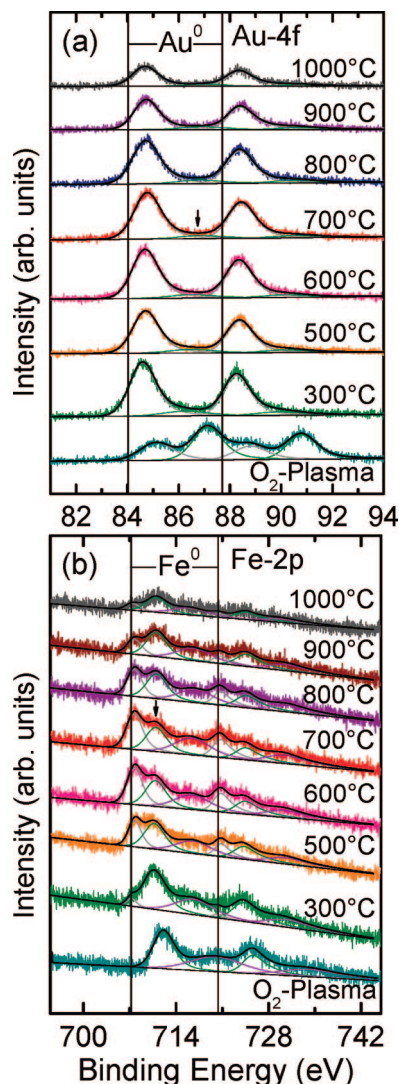


Figure 7. XPS spectra of (a) the Au-4f and (b) Fe-2p core level regions of Au_{0.8}Fe_{0.2} nanoparticles supported on TiO₂(110). The spectra were acquired after O₂ plasma treatment and after subsequent *in situ* annealing from 300–700 °C for 20 min and from 800–1000 °C for 10 min. The arrow in (b) at a BE of 710.5 eV indicates the position of a XPS peak corresponding to the partial formation of an Fe–Au alloy after annealing at 700 °C. Coincidentally, a similar BE is observed for oxidized Fe species and/or FeTiO_{3+δ} compounds at the Fe/TiO₂ interface in pure Fe clusters. The corresponding spectral least-squares fits for the different Au and Fe species are also shown, (solid lines).

et al.⁷³ to reduce 25 nm-thick oxidized Fe-layers. Ethirajan et al.⁷⁴ and Boyen et al.⁷⁵ have also demonstrated that oxidized (O₂–plasma treated) FePt and Co NPs, synthesized by the same inverse micelle encapsulation method used in the present work, can be completely reduced by atomic hydrogen exposure. In our samples, the first H₂–plasma treatment at 300 °C resulted in a reduction of the Fe³⁺ signal, with 28% metallic Fe detected. It should be noted that annealing the same sample at 300 °C immediately after the O₂–plasma treatment (Figure 8b) but without exposure to atomic hydrogen, did not result in any reduction of Fe³⁺ (100% Fe³⁺, Table 1). A subsequent H₂–plasma treatment at 500 °C resulted in further reduction of the Fe–oxide component, but 60% of the total Fe signal at 710.6 eV remained. This experiment shows that the Fe-2p component at 710.6 eV cannot be completely eliminated by hydrogen reduction, indicating that ~60% of that signal is due to partial Au–Fe alloying, Figure 9. By comparison, in the Au_{0.5}Fe_{0.5} NP sample of Figure 8b, after annealing at 500 °C but without a

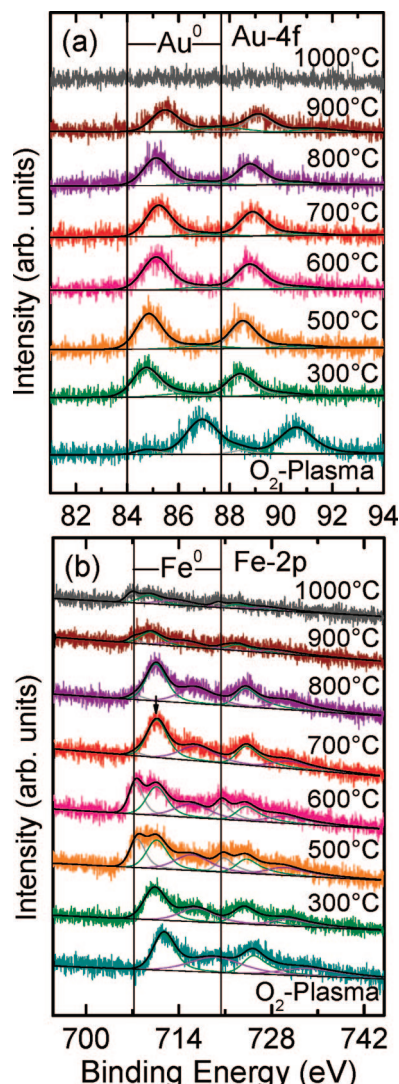


Figure 8. XPS spectra of (a) the Au-4f and (b) Fe-2p core level regions of Au_{0.5}Fe_{0.5} nanoparticles supported on TiO₂(110). The spectra were acquired after O₂ plasma treatment and after subsequent *in situ* annealing from 300–700 °C for 20 min and from 800–1000 °C for 10 min. The arrow in (b) at a BE of 710.7 eV indicates the position of the XPS peak corresponding to Fe in an Fe–Au alloy after annealing at 700 °C. Accidentally, a similar BE is observed for oxidized Fe species and/or FeTiO_{3+δ} compounds at the Fe/TiO₂ interface in pure Fe clusters. The corresponding spectral least-squares fits for the different Au and Fe species are also shown, (solid lines).

simultaneous H₂–plasma treatment, a ~72% Fe signal remained at 710.6 eV. Interestingly, after the last H₂–plasma treatment at 600 °C (Figure 9), an increase in the 710.6 eV Fe component (74%) was observed. On the Au_{0.5}Fe_{0.5} NP sample of Figure 8b, annealed to the same temperature (600 °C) but not H₂–plasma treated, ~71% of the total Fe signal corresponded to the 710.6 eV component. This value is very close to that obtained on the same sample after annealing at 500 °C (~72%). This apparent lack of reduction at the higher temperature is attributed to a compensation effect, since the thermal reduction of Fe₂O₃ at 600 °C is convoluted with an increase in the number of Fe–Au bonds, and consequently leads to an increase of the high BE XPS component at 710.6 eV. Our H₂-reduction experiments indicate that although a slightly enhanced thermal stability of Fe-oxides exists for this bimetallic sample at 500 °C (~12% higher signal of the second Fe component on Au_{0.5}Fe_{0.5} in the absence of H₂), annealing at 600 °C appears to completely reduce the Fe oxides present.

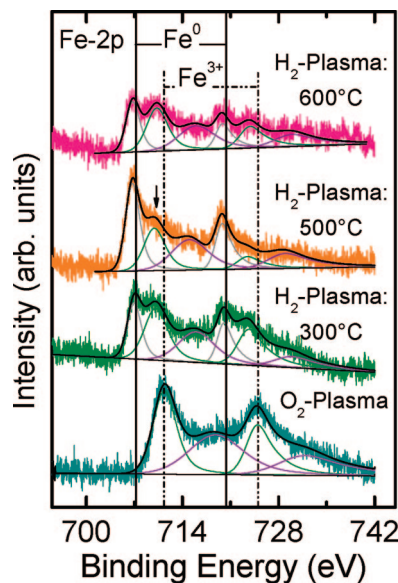


Figure 9. XPS spectra of the Fe-2p core level region from a sample containing $\text{Au}_{0.5}\text{Fe}_{0.5}$ NPs deposited on $\text{TiO}_2(110)$. The sample was first exposed to an O_2 -plasma treatment in UHV for 80 min and subsequently to H_2 -plasma treatments (60 min each) at 300, 500, and 600 °C. At 500 °C, the arrow at a BE of 710 eV indicates the presence of an Au–Fe alloy. The corresponding spectral least-squares fits for the different Fe species are also shown.

Upon further annealing the $\text{Au}_{0.5}\text{Fe}_{0.5}$ NPs from 700 to 900 °C (Figure 8b), the metallic Fe signal (Fe^0) at 707.3 eV has nearly vanished (~10% at 900 °C, Table 1). At 700 °C, only the XPS peak at 710.5 eV can be observed (see arrow in Figure 8b). This change is ascribed to a modification in the coordination of Fe atoms in the $\text{Au}_{0.5}\text{Fe}_{0.5}$ NPs, caused by the complete alloying with Au atoms. The high BE measured for Au at 700 °C (~85.4 eV) also indicates the formation of a $\text{Au}_{0.5}\text{Fe}_{0.5}$ alloy, Figure 8a. From 700 to 800 °C, no additional changes in the BEs of Fe and Au were observed, pointing toward a relatively stable alloy. However, after annealing at 900 °C, a drastic decrease in the Fe XPS signal at 709.8 eV (high BE component) is observed (Fe in $\text{Au}_{0.5}\text{Fe}_{0.5}$ alloy). In parallel, a new XPS peak appears at lower BE (707.3 eV), corresponding to Fe atoms in a less-Au-rich environment, Figure 8b. On the other hand, the intensity of the Au XPS signal did not exhibit such a decrease. Besides, an additional BE shift (+0.3 eV with respect to the value at 800 °C) was measured in the Au-4f signal at 900 °C (85.6 eV), Figure 8a. This effect is attributed to the decrease in the NP size (final state effects) observed by STM after annealing at 900 °C. After annealing at 1000 °C, the nearly complete desorption of gold (within the XPS sensitivity limits, estimated to be approximately 0.3 at. % Au^{76}) was observed in our XPS spectra (Figure 8a), while some iron clusters still remain on the $\text{TiO}_2(110)$ surface. Traces of gold were found on the surface of these NPs by XPS after annealing at 960 °C (not shown).

4. $\text{Au}_{0.2}\text{Fe}_{0.8}$ Nanoparticles. XPS measurements were also conducted on Fe-rich $\text{Au}_{0.2}\text{Fe}_{0.8}$ NPs of similar size, Figure 10. Several important differences with the previous measurements should be noted: (i) a lower onset temperature for Au desorption is observed (>800 °C) as compared to >900 °C for pure Au clusters and $\text{Au}_{0.5}\text{Fe}_{0.5}$ (Au being only slightly more stable than on the pure Au clusters), and >1000 °C for $\text{Au}_{0.8}\text{Fe}_{0.2}$; (ii) significant atomic Fe desorption is observed at/above 800 °C, this being the lowest Fe desorption temperature among all samples investigated; (iii) all Fe atoms in these NPs are incorporated in a Au–Fe alloy above 800 °C.

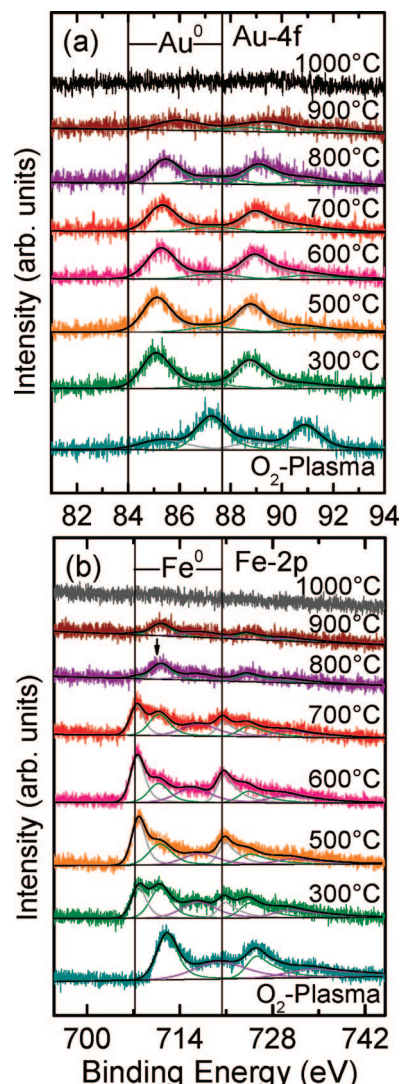


Figure 10. XPS spectra of (a) the Au-4f and (b) Fe-2p core level regions of $\text{Au}_{0.2}\text{Fe}_{0.8}$ nanoparticles supported on $\text{TiO}_2(110)$. The spectra were acquired after O_2 plasma treatment and after subsequent in situ annealing from 300 to 700 °C for 20 min and from 800 to 1000 °C for 10 min. The arrow in (b) at a BE of 710.5 eV indicates the position of the XPS peak corresponding to Fe in a Fe–Au alloy after annealing at 800 °C. Coincidentally, a similar BE is observed for oxidized Fe species and/or $\text{FeTiO}_{3+\delta}$ compounds at the Fe/TiO_2 interface in pure Fe clusters. The corresponding spectral least-squares fits for the different Au and Fe species are also shown.

Discussion

A. Morphology (AFM, STM). Our AFM and STM images (Figures 1–3) demonstrate that our preparation technique results in self-assembled size-selected $\text{Au}_x\text{Fe}_{1-x}$ nanoparticles. The average NP heights of Au, Fe and $\text{Au}_x\text{Fe}_{1-x}$ are centered in a narrow range (e.g., at ~3.5–4.5 nm after UHV annealing at 300 °C, Figure 5a) and show insignificant changes with annealing up to 700 °C. Further, the NP height distributions are relatively narrow with standard deviations in the range of $\sim \pm 1.2$ to ± 1.8 nm, Figure 5a. Similar observations can be made for the average interparticle distances, which are centered at ~ 38 –47 nm, Figure 5b, with standard deviations ranging from $\sim \pm 9$ to ± 10 nm. Moreover, the spatial autocorrelation plots in Figure 2b,d (averaged over the sample areas shown in Figure 2a,c) provide evidence for the quasi-hexagonal spatial arrangement of the NPs. All of these observations show that our self-assembled NPs have regular interparticle spacing and are size-selected.

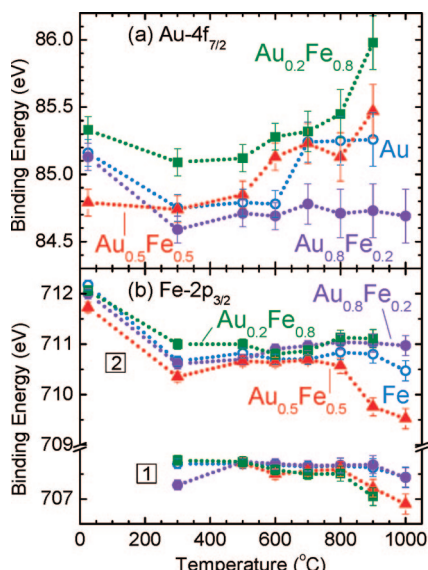


Figure 11. Evolution of the (a) Au-4f_{7/2} and (b) Fe-2p_{3/2} binding energies of Au (○), Fe (○), and Au_xFe_{1-x} [x = 0.8 (●), 0.5 (▲), 0.2 (■)] nanoparticles supported on TiO₂(110) with annealing temperature. In (b), the component labeled as 1 corresponds to metallic Fe (Fe-2p_{3/2} BE of 706.9–707.7 eV), while component 2 (Fe-2p_{3/2} BE of 709.8–712.2 eV) includes Fe–oxides + FeTiO_{3+δ} + Au–Fe alloy compounds, which cannot be distinguished based on the BE. These data were extracted from the XPS spectra displayed in Figures 6, 7, 8, and 10.

Our AFM and STM images (Figures 1–3) as well as the results shown in Figure 5 provide proof for the high thermal stability of mono and bimetallic nanoparticles prepared by inverse micelle encapsulation and deposited on TiO₂(110). It should be noted that the height of the Fe NPs was found to decrease above 700 °C, while the Au and Au_{0.5}Fe_{0.5} NP heights decrease only above 900 °C. This difference could be related to changes in the TiO₂ morphology originating from the distinct interaction of Fe versus Au with TiO₂ (e.g., Fe encapsulation by TiO_x). Interestingly, the changes in the TiO₂ morphology observed at 900 °C, Figure 3d,h, do not significantly alter the initial arrangement of the NPs, providing evidence for a strong NP/support adhesion. This is an important factor for catalysis applications, since the longevity of a catalyst is largely determined by its morphological stability under reaction conditions (e.g., high temperature). Recently, Matthey et al.⁷⁷ observed that UHV-evaporated Au clusters supported on reduced TiO₂(110) exhibit a clear tendency toward sintering, while similar clusters deposited on an oxidized TiO₂(110) surface displayed a stronger adhesion and stability. Since our TiO₂(110) surface is significantly reduced at 900 °C (the presence of a Ti³⁺ component with binding energy of 457.8 eV can be seen in Suppl. Figure 4, Supporting Information), the stability of our NPs must have a different origin. This should be investigated in more detail in the future.

B. Electronic and Chemical Characterization (XPS).

1. Size and Support Effects. Figure 11 summarizes the evolution of the Au-4f_{7/2} (a) and Fe-2p_{3/2} (b) binding energies extracted from the XPS spectra in Figures 6, 7, 8, and 10.

In our pure Au NP samples, Au-4f binding energy shifts of +0.8–1.3 eV (relative to bulk Au, 84.0 eV) were detected. Similar positive BE shifts were previously observed by Chusuei et al.⁴⁷ and Howard et al.⁶⁵ on Au clusters evaporated on TiO₂(110) at room temperature. It has been reported that the magnitude of these shifts strongly depends on the particle size⁴⁷ as well as on the structure and stoichiometry of the TiO₂ support, both of which change upon high temperature annealing.⁶⁵ The

origin of these shifts is commonly assigned to either initial state effects (changes in the electronic structure of NPs with decreasing size) or to final state effects (insufficient screening of the positive charge left behind during the photoemission process) and NP charging.^{45,47,64,65} Shifts of similar origin were also observed in the XPS spectra of our pure Fe NPs. In particular, a BE shift of up to +0.7 eV with respect to bulk Fe⁰ at 707.1 eV^{48,49} was detected for the low BE Fe component in the Fe NPs.

The Au-4f binding energies in the Au_{0.5}Fe_{0.5}, and Au_{0.2}Fe_{0.8} NP samples are slightly higher than those obtained for the pure Au NPs, but follow the same trend of increasing BE with increasing annealing temperature, Figure 11a. The large Au-4f BEs observed for these samples at 900 °C (up to 86 eV for Au_{0.2}Fe_{0.8} and 85.3 eV for pure Au clusters as compared to bulk Au at 84 eV) can be attributed to a decrease in the particle size due to partial Au desorption from the NPs. Although for the bimetallic samples the formation of a Au–Fe alloy might also contribute to the observed Au-4f BE increase, such an effect is not considered dominant, since the temperature-dependent trends observed in the Au-4f BEs were not found to correlate with those of the Fe-2p signals, Figure 11b. Interestingly, the Au-4f BE of the Au_{0.8}Fe_{0.2} NPs was found to remain nearly constant throughout the entire temperature range. This sample also demonstrated the highest stability against Au desorption (a clear Au signal was detected after annealing at 1000 °C), suggesting that the increase in the BE of the pure Au NPs and the other bimetallic samples may be attributed to a decrease in the NP size.

2. Stability of Fe–Oxide and/or TiO_x Encapsulation. The thermal evolution of the binding energy of the two Fe-2p components of our mono- and bimetallic samples is shown in Figure 11b. In this graph, the low BE component (706.9 eV–707.7 eV) labeled as 1 corresponds to metallic Fe, while component 2 (709.6–712.2) is assigned to Fe–oxides, and/or FeTiO_{3+δ} compounds, and/or a Au–Fe alloy. The first component appears at 300 °C after an initial Fe₂O₃ reduction, and its BE remains nearly constant up to 800 °C. The presence of this component in all bimetallic samples indicates that complete Au–Fe alloying was not achieved at any given temperature. Sample annealing above 800 °C results in a slight decrease of the BE of this component for the bimetallic NPs, while it remains nearly constant for the pure Fe NPs. The BE of the second component (high BE, labeled as 2) initially decreases up to 500 °C signifying the reduction of Fe–oxide complexes. However, it remains nearly constant from 500 °C up to 800 °C for all samples, indicating the presence of interfacial FeTiO_{3+δ} compounds (pure Fe NPs) and/or an Au–Fe alloy component. A significant decrease in the BE of this second component above 800 °C is only observed for the Au_{0.5}Fe_{0.5} sample. As will be discussed in more detail later, this effect indicates Au–Fe phase separation.

The presence of the high-BE shoulder in the XPS spectra of the pure Fe NPs at ~710.5 eV (arrow in Figure 6b and component 2 in Figure 11b) upon annealing at/above 500 °C could be indicative of the enhanced thermal stability of Fe–oxides in these clusters, as well as of the formation of FeTiO_x compounds. Since previous TEM studies reported the decomposition of Fe₂O₃ on the surface of pure Fe nanoparticles [Fe₂O₃ shell(2 nm)/bcc-Fe core(5 nm)] at about 500 °C,⁷² the presence of FeTiO_x species in our annealed samples must be considered. The latter explanation for our high BE component in the pristine Fe NPs is in agreement with XPS⁵¹ and ultraviolet photoelectron spectroscopy⁷⁸ data on ultrathin Fe films on TiO₂(110). Ternary

oxides such as FeTiO_3 are likely to form at the particle-substrate interface.⁵¹ Fuji et al.⁵² reported binding energies of 709 eV (Fe^{2+}) for bulk FeTiO_3 , and 711 eV (Fe^{3+}) for $\text{FeTiO}_{3+\delta}$ compounds. Our 710.5 eV BE (shoulder in Figure 6b, arrow) might indicate the formation of nonstoichiometric $\text{FeTiO}_{3+\delta}$ compounds. Furthermore, the observation by Fuji et al.⁵² of a weak high BE components (Fe^{3+}) in the Fe-2p XPS spectra of stoichiometric FeTiO_3 films (dominated by Fe^{2+}) was ascribed to intervalence charge transfer ($\text{Fe}^{2+} + \text{Ti}^{4+} \rightarrow \text{Fe}^{3+} + \text{Ti}^{3+}$).⁵² In addition, according to the work by Pan et al.⁵¹ and Diebold et al.⁶⁶ on UHV evaporated Fe islands deposited on $\text{TiO}_2(110)$, the possibility of encapsulation of our Fe nanoparticles by TiO_x upon annealing should also be considered. Nearly complete TiO_x encapsulation of Fe was reported in the temperature range of 500–700 °C upon several hours of annealing in UHV.⁵¹ Interestingly, despite the encapsulation, the Fe particles in this study were found to be in the metallic state, with the exception of the interfacial Fe atoms. Although from our XPS data we cannot exclude the possibility of Fe encapsulation by TiO_x , one should keep in mind that the shapes of UHV grown (mainly flat 2D islands⁵¹) and micellar (3D spherical) clusters are different and that cluster/support interactions in these two systems might also be different. In addition, the previous studies^{51,66} reported the Fe encapsulation by TiO_x after several hours of annealing in UHV, while in our study the annealing times were much shorter (10–20 min) and therefore the encapsulation less likely. In order to clarify this aspect, additional spectroscopic (STS) studies are currently being conducted in our group and will be published elsewhere. Previous STS data by Dulub et al.⁷⁹ on UHV evaporated Pt clusters deposited on $\text{TiO}_2(110)$ indicated the appearance of a bandgap in Pt regions after sample annealing up to a maximum temperature of 700 °C. The authors attributed this bandgap to the encapsulation of Pt by an ultrathin TiO_x film. Some preliminary STS data on $\text{Au}_{0.5}\text{Fe}_{0.5}$ NPs deposited on $\text{TiO}_2(110)$ can be found in our previous work.⁵ For this bimetallic sample, no bandgap was observed in the current–voltage curves measured after annealing at 700 °C on the top of our $\text{Au}_{0.5}\text{Fe}_{0.5}$ NPs (below the onset temperature of Au segregation to the NP surface at about 800 °C), suggesting the lack of significant encapsulation by TiO. A more exhaustive study focused on this aspect is still needed to rule out this possibility with certainty.

The second Fe-2p BE component (labeled as 2 in Figure 11b) is also present for all bimetallic samples, and as can be seen in Figure 12, its relative contribution to the total Fe XPS signal is higher than in the case of the monometallic (pure) Fe sample at elevated annealing temperatures. This result could have two different origins: (i) the enhanced stability of FeO_x or FeTiO_x compounds in the presence of Au, and/or (ii) the formation of a Au–Fe alloy. The latter point is considered to be the main factor responsible for the high BE Fe component observed for these samples at elevated temperatures, and will be discussed in the next section. Based on our H_2 -reduction experiments on $\text{Au}_{0.5}\text{Fe}_{0.5}$ NPs, it appears that only a slightly enhanced stability of Fe–oxide species is present for our samples at 500 °C, and that above that temperature, the second Fe component should be attributed to the formation of a Au–Fe alloy as well as to interfacial FeTiO_x compounds. The mechanism by which the presence of Au impurities could help stabilize oxidized Fe compounds at 500 °C is unclear, but could be related to the low affinity of Au for O, to the presence of subsurface Fe–oxide, to the reduction of the FeO_x –Au interfacial energy, or to strain relaxation in the FeO_x film on the Au–Fe NP due to a change in the average lattice parameter. The effect of a secondary metal

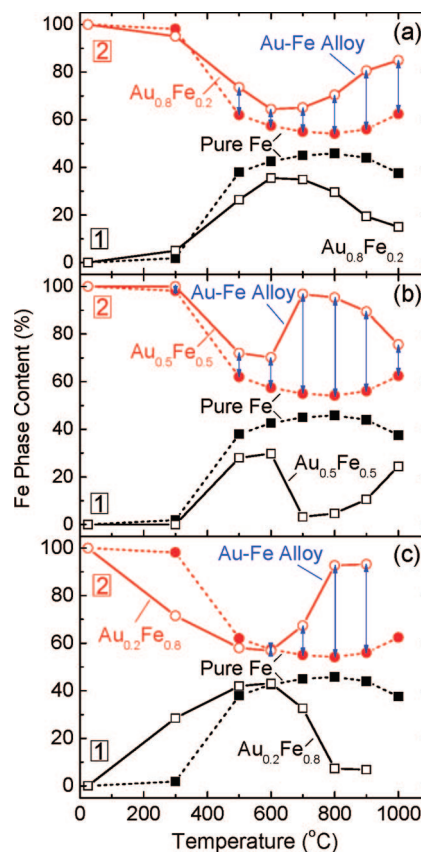


Figure 12. Evolution of the relative content (spectral area) of the two different Fe phases (component 1 and component 2) obtained from the fits of Fe-2p XPS spectra acquired after sample annealing in UHV from RT to 1000 °C. The data shown correspond to the following samples: (a) $\text{Au}_{0.8}\text{Fe}_{0.2}$, (b) $\text{Au}_{0.5}\text{Fe}_{0.5}$, and (c) $\text{Au}_{0.2}\text{Fe}_{0.8}$ NPs, (□ and ○ connected by solid lines). For comparison, the phase content of the pure Fe NPs is also plotted (■ and ● connected by dashed lines). The component labeled as 1 (squares) corresponds to the low BE feature ($\text{Fe}-2\text{p}_{3/2}$ at 706.9–707.7 eV) assigned to metallic Fe, while component 2 corresponds to the high BE feature ($\text{Fe}-2\text{p}_{3/2}$ at 709.8–712.2 eV and satellites at ~720 eV) attributed to Fe–oxides + $\text{FeTiO}_{3+\delta}$ compounds + Au–Fe alloy. These data were extracted from the XPS spectra displayed in Figures 6, 7, 8, and 10. The vertical arrows indicate the increase in the phase content of component 2 in the AuxFel-x nanoparticles relative to the phase content of component 2 in the pure Fe NPs. This increase is attributed to the formation of an Au–Fe alloy.

on the stability of Pt oxides in similarly synthesized bimetallic $\text{Pt}_{0.8}\text{M}_{0.2}$ ($\text{M} = \text{Fe}, \text{Ru}, \text{Pd}, \text{Au}$) nanoparticles has been recently reported by Croy et al.⁸⁰ based on XPS investigations. In this study, the largest amount of PtO was present in the samples that contained a secondary metal that did not have a high affinity for O (in this example Au in Pt–Au NPs), and a slightly higher content of PtO was observed in the Pt–Au NPs as compared to pure Pt NPs.⁸⁰

3. Au–Fe Alloy Formation. Figure 12 summarizes the thermal evolution of the relative content of the two Fe species (components 1 and 2) present in our bimetallic samples: (a) $\text{Au}_{0.8}\text{Fe}_{0.2}$, (b) $\text{Au}_{0.5}\text{Fe}_{0.5}$, and (c) $\text{Au}_{0.2}\text{Fe}_{0.8}$ NPs, (open squares and open circles connected by solid lines). For comparison purposes, the phase contents obtained for the pure Fe NPs are also plotted (closed squares and closed circles connected by dashed lines). In analogy to Figure 11, the low BE component labeled as 1 corresponds to metallic Fe, while component 2 is assigned to Fe–oxides, and/or $\text{FeTiO}_{3+\delta}$ compounds, and/or a Au–Fe alloy. If one considers that the presence of Au in the Au–Fe NPs does not significantly alter the stability of oxidized

Fe species above 500 °C, the difference in the total content of component 2 in our bimetallic NPs with respect to the pure Fe NPs (indicated in Figure 12 by arrows) can be attributed to the formation of a partial Au–Fe alloy.

The behavior displayed in Figure 12a for both Fe components in the Au_{0.8}Fe_{0.2} NPs is similar to the pure Fe NPs, although a clear increase in the concentration of the high BE Fe component 2 (assigned to Fe-oxide/FeTiO_x/Au–Fe), combined with a decrease of the concentration of component 1, is observed in the bimetallic sample above 500 °C, contrary to the case of the pure Fe NPs. This indicates that in addition to the presence of segregated metallic Fe grains (component 1), increasing partial Au–Fe alloying occurs at and above 500 °C.

The thermal evolution of the two Fe components (1 and 2) in the bimetallic samples with higher Fe content is also drastically different from that of the pure Fe NPs. In particular, a strong decrease in the content of metallic Fe (component 1), combined with a strong increase of the content of component 2 (Au–Fe alloy), is observed above 600 °C for the Au_{0.5}Fe_{0.5} (Figure 12b) and Au_{0.2}Fe_{0.8} (Figure 12c) NP samples, indicating a higher degree of Au–Fe interaction and alloying. In the temperature range of 600–800 °C, the majority phase in the Au_{0.5}Fe_{0.5} NPs was found to be a Au–Fe alloy. This result is in agreement with our previous STS data on Au_{0.5}Fe_{0.5} NPs,⁵ where phase-segregated structures (separated Au and Fe grains) were present at 300 °C, and phase segregation into pure bcc-Fe and a Au–Fe solid-solution (alloy) was found to be present up to 600 °C. At 700 °C the formation of a Au–Fe alloy was also observed by STS.⁵ The increase in the content of the Au–Fe alloy component is more gradual in the case of the Au_{0.2}Fe_{0.8} NPs, and is shifted to higher temperatures, with a majority Au–Fe alloy phase in the range of 800–900 °C.

The trends described above show a clear difference with the behavior expected from the currently known bulk phase diagrams. According to the Fe–Au phase diagram for a bulk alloy with an average composition of 50 at. % Fe (and 50 at. % Au),⁸¹ a phase segregation would occur at 300 °C, resulting in nearly pure bcc Fe and in a Au-rich fcc Au–Fe alloy containing roughly 4 at. % Fe. However, the phase separation line on the Au-rich side is not well-known. If the temperature is increased to 700 °C, such an alloy would segregate into a bcc Fe–Au alloy containing ~1 at. % Au, and in a fcc Au–Fe alloy with 40 at. % Fe. For 50 at. % Fe, a temperature of at least 800 °C is required in order to form a solid solution (alloy) of fcc Fe_{0.5}Au_{0.5}. This occurs for example at 900 °C. A comparison with our results obtained for nanoparticles with nominally 50 at. % Fe, shows that the phase diagram is shifted to lower temperatures as compared to bulk Au–Fe alloys. For instance, our results indicate the formation of a Au–Fe alloy (solid solution) in the Au_{0.5}Fe_{0.5} nanoparticles at 700 °C, which is lower than the value of 800 °C for bulk alloys of the same composition.

4. Au–Fe Phase Separation and Au Segregation to the NP Surface. As can be seen in Figure 12b, after the formation of a Au–Fe alloy, further annealing above 800 °C results in a sudden increase of the metallic Fe content (component 1) for the Au_{0.5}Fe_{0.5} NPs, while the metallic Fe content for the Au_{0.2}Fe_{0.8} NPs does not drop further, but stabilizes at 900 °C (Figure 12c). This effect (and the associated decrease in the high BE Fe component) is attributed to Au–Fe phase separation. Surprisingly, after annealing up to 1000 °C, no signs of phase separation can be observed by XPS on the Au_{0.8}Fe_{0.2} NPs, Figure 12a, since the content of the high BE Fe component 2 remains

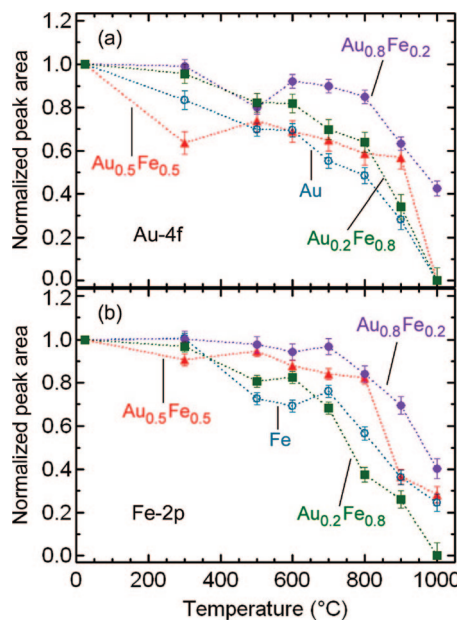


Figure 13. Evolution of the (a) Au-4f and (b) Fe-2p XPS normalized spectral areas (integrated intensities) of Au (○), Fe (△), and Au_xFe_{1-x} [x = 0.8 (■), 0.5 (▲), 0.2 (●)] nanoparticles supported on TiO₂(110) with annealing temperature. These data were extracted from the XPS spectra displayed in Figures 6, 7, 8, and 10. The spectral areas were calculated from the least-squares fits of the XPS peaks using the Casa-XPS software considering a linear background and a Gaussian–Lorentzian line-shape. The data are normalized using the respective XPS spectral area measured directly after O₂–plasma treatment as reference.

nearly stable from 900–1000 °C and is clearly higher than at lower temperatures.

Our *in situ* temperature-dependent XPS data can also be used to extract information about atomic segregation within our NPs after Au–Fe phase separation as well as the possible encapsulation by ultrathin TiO_x films. The Au-4f and Fe-2p integrated intensities have been plotted in Figure 13 as a function of the annealing temperature. The data are normalized using the respective XPS spectral area measured directly after O₂–plasma treatment as reference. For all samples a general decrease in the Au-4f XPS signal was observed with increasing annealing temperature, Figure 13a. However, while the Au signal in pure Au NPs decreases nearly monotonically with temperature, enhanced stability and a slower decay rate was observed on the bimetallic clusters. Specifically, at 900 °C the largest normalized Au signals were measured on the Au_{0.8}Fe_{0.2} and Au_{0.5}Fe_{0.5} NPs, and at 1000 °C a gold signal was detected only for the Au_{0.8}Fe_{0.2} NPs. This difference indicates that the presence of Fe stabilizes Au atoms in these Au-rich bimetallic clusters, minimizing Au desorption. In addition, the possibility of Au segregation to the NP surface should be taken into consideration, since higher Au signals will be measured by XPS when the Au atoms reside at the NP surface. As an example, for the Au_{0.5}Fe_{0.5} NPs only a negligible reduction in the Au signal (2%) was measured going from 800 to 900 °C, Figure 13a, while a much larger decrease (46%) is evident in the Fe signal of this sample in the same temperature range, Figure 13b. This result is consistent with Au atoms segregating to the Au_{0.5}Fe_{0.5} NP surface, damping the XPS signal from Fe atoms closer to the NP core.

The decrease in the Fe XPS signal observed in Figure 13b for the bimetallic samples above 600–700 °C could be ascribed to four different origins: (i) the desorption of Fe atoms, (ii) the segregation of Au atoms to the surface of the NPs, (iii) the migration of Fe atoms into the TiO₂ support, (iv) the encapsula-

tion of Fe by TiO_x . The diffusion of Au atoms to the surface will induce the attenuation of the photoelectrons arising from the underlying Fe atoms which in turn decreases the Fe XPS signal. If Au segregation to the NP surface is the origin of the reduction in the Fe signal, this is expected to be accompanied by a partial decomposition of the gold–iron alloy phase (solid solution) at 900 °C. The latter fact is in agreement with the remarkable increase of the metallic Fe component 1 (707.6 eV) above 800 °C for the $\text{Au}_{0.5}\text{Fe}_{0.5}$ (Figure 12b) and the constancy (instead of a further drop) of this Fe signal at 900 °C for the $\text{Au}_{0.2}\text{Fe}_{0.8}$ NP samples (Figure 12c). The segregation of gold can be driven by the tendency of the Au–Fe NPs to lower their surface free energy by altering the composition of their surface. Since Au has a much lower surface energy ($\gamma_{\text{Au}} = 1.61 \text{ J/m}^2$) than Fe ($\gamma_{\text{Fe}} = 3.28 \text{ J/m}^2$),⁸² the segregation of Au atoms to the NP surface upon annealing in an oxygen-depleted environment (UHV) is likely. Since an analogous, strong reduction in the Fe XPS signal above 700 °C was also observed for the gold-free Fe NPs, Figure 13b, the desorption of Fe atoms or the diffusion of Fe atoms into the $\text{TiO}_2(110)$ substrate, should also be considered. As was mentioned before, the encapsulation of Fe by TiO_x is unlikely due to the short annealing times used in the present study.

5. Au and Fe Desorption. For the pure Au NPs, the monotonic decrease in the Au signal observed upon annealing, Figure 13a, and its complete disappearance at 1000 °C is attributed to the desorption of Au. A decrease in the Au XPS signal could also be a result of Au encapsulation by TiO_x . However, such an effect is excluded due to the low affinity of Au for O, the high positive heat of formation of Au–Ti alloys, and previous data by Zhang et al.⁸³ demonstrating the lack of encapsulation of Au by TiO_2 .

From the XPS integrated area, Figure 13, we estimate that the onset of Au desorption from the $\text{Au}_{0.8}\text{Fe}_{0.2}$ NPs occurs above 800 °C, since only a ~15% decrease in the Au signal was measured below 800 °C, and a much stronger decrease above 900 °C. Surprisingly, as Figure 13 shows, at and above 900 °C the gold signal from the $\text{Au}_{0.8}\text{Fe}_{0.2}$ clusters (Figure 7a) is significantly higher than that of similarly sized pure Au clusters annealed under identical conditions, Figure 6a. Furthermore, although nearly complete Au desorption (within the resolution of XPS) was observed on the pure Au clusters at 1000 °C (Figure 6a), a clear gold signal was measured on the $\text{Au}_{0.8}\text{Fe}_{0.2}$ NPs at 1000 °C (being ~43% of the Au signal detected on this sample at 300 °C). This observation suggests the positive effect of small amounts of Fe (nominally 20 at. %) on the thermal stability of Au in our Au-rich NPs.

Contrary to the case of the $\text{Au}_{0.8}\text{Fe}_{0.2}$ NPs, the complete desorption of Au from our $\text{Au}_{0.5}\text{Fe}_{0.5}$ and $\text{Au}_{0.2}\text{Fe}_{0.8}$ NPs occurred in the temperature range of 960 to 1000 °C. Such temperatures are in agreement with TPD experiments conducted by Chen et al.,⁸⁴ who observed a maximum Au desorption peak at ~977 °C for a 3.4 ML-thick gold film deposited on a $\text{TiO}_x/\text{Mo}(112)$ surface. The authors mentioned that the desorption of Au occurred in the form of Au dimers. Similarly, Yi et al.⁴² observed the desorption of Au from Pd–Au surfaces in the temperature range of [927 °C – 1027 °C]. According to refs 51 and 84–96, the dissociation (or bond) energies of Au_2 , Fe_2 , Au–Fe, Au–Ti and Fe–Ti dimers are: ~2.02 eV (DFT) and ~2.30 eV (exp) for Au–Au, ~1.20 eV (DFT) and ~1.14 eV (exp) for Fe–Fe, ~1.79 eV (DFT) and ~1.95 eV (exp) for Au–Fe, ~2.52 eV (DFT) and ~2.15 eV (exp) for Au–Ti, 2.6 eV (exp) for Fe–Ti. Although the reported energies vary significantly depending on the reference consulted, the most stable bonds appear to be those

between Au–Ti, Au–Au, and Au–Fe atoms, followed by Fe–Ti and Fe–Fe. Since Fe encapsulation by TiO_x has been suggested in the past,^{66,97} the presence of Fe in our Au–Fe nanoparticles could lead to an enhanced Au–Ti interaction that might stabilize the Au atoms against thermal desorption. In addition, since the bond energy of Au–Fe is higher than that of Fe–Fe dimers, it is expected that the presence of Au in these bimetallic clusters helps to stabilize the Fe atoms.

Although theoretical simulations are necessary to fully understand the concentration-dependence of the thermal stability of $\text{Au}_x\text{Fe}_{1-x}$ NPs, with $\text{Au}_{0.8}\text{Fe}_{0.2}$ being particularly stable, a tentative mechanism is described below. First, the higher melting temperature of Fe ($T_m = 1535$ °C) as compared to Au ($T_m = 1064$ °C) could induce an upward shift of the Au melting temperature once an alloy is formed. Second, the diffusion of Au atoms to the surface of the Au–Fe NPs, owing to its lower surface energy and higher atomic volume ($V_{\text{Au}} = 12.5 \text{ \AA}^3$) compared with those of Fe, $V_{\text{Fe}} = 8.0 \text{ \AA}^3$), may reduce the mechanical stress on the atoms at the NP's core (presumably Fe-rich upon high temperature annealing), enhancing the NP stability. For example, Rodriguez-Lopez et al.³⁸ have observed that the substitution of the central Ag atom in an Ag_{55} cluster by a smaller atom such as Ni or Cu increases the melting temperature of the $\text{Ag}_{54}\text{Ni}_1$ and $\text{Ag}_{54}\text{Cu}_1$ clusters by 50 and 30 K, respectively.³⁸ The authors explain this effect based on a decrease in the stress at the core of the small Ag clusters that seems to stabilize these clusters against thermal disordering.³⁸

Conclusions

The thermal evolution of the morphological and electronic properties of bimetallic $\text{Au}_x\text{Fe}_{1-x}$ NPs supported on $\text{TiO}_2(110)$ has been investigated *in situ* via STM and XPS. The STM measurements revealed that Au–Fe NPs prepared by diblock copolymer encapsulation and self-assembled on $\text{TiO}_2(110)$ exhibit a remarkable stability against geometric disorder. In fact, the initial hexagonal arrangement was preserved up to an annealing temperature of 900 °C.

XPS measurements were used to gain understanding on the onset of Au–Fe alloy formation and segregation or encapsulation phenomena in nanoparticles with similar average size but distinct composition. In general, with increasing annealing temperature, four types of structures were inferred in a nanoparticle: (i) segregated Fe and Au grains, (ii) a heterogeneous mixture of fcc–Au–Fe alloy (majority phase) plus bcc Fe phase (minority phase), (iii) an Fe-rich core (bcc–Fe) and a Au-rich surface, (iv) an Fe–Ti–O alloy after gold desorption. Fe encapsulation by TiO_x is unlikely in our nanoparticle samples due to our short annealing times.

As expected from the bulk phase diagram of Au and Fe, for a given particle size distribution, the onset temperature for these four regions strongly depends on the initial Au/Fe ratios. Our study highlighted the remarkably high thermal stability of Au in $\text{Au}_{0.8}\text{Fe}_{0.2}$ NPs (up to 1000 °C), as compared to the pure Au, $\text{Au}_{0.5}\text{Fe}_{0.5}$, and $\text{Au}_{0.2}\text{Fe}_{0.8}$ NPs, where Au was found to desorb above 900 °C. This effect is tentatively attributed to a possible release of core stress upon Au segregation to the NP surface. Detailed molecular dynamics studies are needed to fully understand the origin of the enhanced thermal stability of certain Au–Fe nanoparticle compositions.

Acknowledgment. Helpful discussions with Prof. Werner Keune (University of Duisburg-Essen) and Prof. Pieter G. Kik (University of Central Florida) are greatly appreciated. This

work was made possible thanks to the financial support of the National Science Foundation (NSF-CAREER, Award N. 0448491).

Supporting Information Available: Supplemental Figures 1–4. This material is available free of charge via the Internet at <http://pubs.acs.org>.

References and Notes

- (1) Campbell, C. T. *Annu. Rev. Phys. Chem.* **1990**, *41*, 775.
- (2) Rodriguez, J. A. *Surf. Sci. Rep.* **1996**, *24*, 225.
- (3) Sinfelt, J. H. *Bimetallic Catalysts*; Wiley: New York, 1983.
- (4) Besenbacher, F.; Chorkendorff, I.; Clausen, B. S.; Hammer, B.; Molenbroek, A. M.; Norskov, J. K.; Stensgaard, I. *Science* **1998**, *279*, 1913.
- (5) Naitabdi, A.; Roldan Cuena, B. *Appl. Phys. Lett.* **2007**, *91*, 113110.
- (6) Carlsson, A. F.; Naschitzki, M.; Baumer, M.; Freund, H. J. *J. Phys. Chem. B* **2003**, *107*, 778.
- (7) Molenbroek, A. M.; Norskov, J. K.; Clausen, B. S. *J. Phys. Chem. B* **2001**, *105*, 5450.
- (8) Xu, Y.; Ruban, A. V.; Mavrikakis, M. *J. Am. Chem. Soc.* **2004**, *126*, 4717.
- (9) Gleich, B.; Ruff, M.; Behm, R. J. *Surf. Sci.* **1997**, *386*, 48.
- (10) Liu, P.; Norskov, J. K. *Phys. Chem. Chem. Phys.* **2001**, *3*, 3814.
- (11) Park, J. Y.; Zhang, Y.; Grass, M.; Zhang, T.; Somorjai, G. A. *Nano Lett.* **2008**, *8*, 673.
- (12) Chiang, I. C.; Chen, D. H. *Adv. Funct. Mater.* **2007**, *17*, 1311.
- (13) Chang, W. S.; Park, J. W.; Rawat, V.; Sands, T.; Lee, G. U. *Nanotechnology* **2006**, *17*, 5131.
- (14) Lu, D. L.; Domen, K.; Tanaka, K. *Langmuir* **2002**, *18*, 3226.
- (15) Saha, D. K.; Koga, K.; Takeo, H. *Eur. Phys. J. D* **1999**, *9*, 539.
- (16) Wang, L. Y.; Luo, J.; Maye, M. M.; Fan, Q.; Qiang, R. D.; Engelhard, M. H.; Wang, C. M.; Lin, Y. H.; Zhong, C. J. *J. Mater. Chem.* **2005**, *15*, 1821.
- (17) Sun, Q.; Kandalam, A. K.; Wang, Q.; Jena, P.; Kawazoe, Y.; Marquez, M. *Phys. Rev. B* **2006**, *73*, 134409.
- (18) Lee, Y. P.; Kudryavtsev, Y. V.; Nemoshkalenko, V. V.; Gontarz, R.; Rhee, J. Y. *Phys. Rev. B* **2003**, *67*, 104424.
- (19) Takanashi, K.; Mitani, S.; Sano, M.; Fujimori, H.; Nakajima, H.; Osawa, A. *Appl. Phys. Lett.* **1995**, *67*, 1016.
- (20) Takanashi, K.; Mitani, S.; Himi, K.; Fujimori, H. *Appl. Phys. Lett.* **1998**, *72*, 737.
- (21) Haruta, M.; Yamada, N.; Kobayashi, T.; Iijima, S. *J. Catal.* **1989**, *115*, 301.
- (22) Finch, R. M.; Hodge, N. A.; Hutchings, G. J.; Meagher, A.; Pankhurst, Q. A.; Siddiqui, M. R. H.; Wagner, F. E.; Whyman, R. *Phys. Chem. Chem. Phys.* **1999**, *1*, 485.
- (23) Gasior, M.; Grzybowska, B.; Samson, K.; Ruszel, A.; Haber, J. *Catal. Today* **2004**, *91*–92, 131.
- (24) Cameron, D.; Holliday, R.; Thompson, D. *J. Power Sources* **2003**, *118*, 298.
- (25) Milone, C.; Ingoglia, R.; Pistone, A.; Neri, G.; Galvagno, S. *Catal. Lett.* **2003**, *87*, 201.
- (26) Tsioncheva, T.; Tvanova, L.; Lotz, A. R.; Smatt, J. H.; Dimitrov, M.; Paneva, D.; Mitov, I.; Linden, M.; Minchev, C.; Froba, M. *Catal. Commun.* **2007**, *8*, 1573.
- (27) Molenbroek, A. M.; Haukka, S.; Clausen, B. S. *J. Phys. Chem. B* **1998**, *102*, 10680.
- (28) Yuge, K.; Seko, A.; Kuwabara, A.; Oba, F.; Tanaka, I. *Phys. Rev. B* **2007**, *76*, 045407.
- (29) Nakajima, H.; Takanashi, K.; Mitani, S.; Fujimori, H. *Mater. Trans., JIM* **1998**, *39*, 1180.
- (30) Wang, G. F.; Van Hove, M. A.; Ross, P. N.; Baskes, M. I. *Prog. Surf. Sci.* **2005**, *79*, 28.
- (31) Creemers, C.; Deurinck, P.; Helfenstein, S.; Luyten, J. *Appl. Surf. Sci.* **2003**, *219*, 11.
- (32) Zarkevich, N. A.; Tan, T. L.; Johnson, D. D. *Phys. Rev. B* **2007**, *75*.
- (33) Ma, Y. G.; Balbuena, P. B. *Surf. Sci.* **2008**, *602*, 107.
- (34) Sahoo, S.; Rollmann, G.; Entel, P. *Phase Transit.* **2006**, *79*, 693.
- (35) Xiao, S.; Hu, W.; Luo, W.; Wu, Y.; Li, X.; Deng, H. *Eur. Phys. J. B* **2006**, *54*, 479.
- (36) Rodriguez-Lopez, J. L.; Montejano-Carrizales, J. M.; Jose-Yacaman, M. *Appl. Surf. Sci.* **2003**, *219*, 56.
- (37) Christensen, A.; Stoltze, P.; Norskov, J. K. *J. Phys.: Condens. Mat.* **1995**, *7*, 1047.
- (38) Mottet, C.; Rossi, G.; Baletto, F.; Ferrando, R. *Phys. Rev. Lett.* **2005**, *95*, 035501.
- (39) Huang, S. P.; Balbuena, P. B. *J. Phys. Chem. B* **2002**, *106*, 7225.
- (40) Rodriguez-Lopez, J. L.; Montejano-Carrizales, J. M.; Pal, U.; Sanchez-Ramirez, J. F.; Troiani, H. E.; Garcia, D.; Miki-Yoshida, M.; Jose-Yacaman, M. *Phys. Rev. Lett.* **2004**, *92*, 196102.
- (41) Ramirez-Caballero, G. E.; Balbuena, P. B. *Chem. Phys. Lett.* **2008**, *456*, 64.
- (42) Yi, C. W.; Luo, K.; Wei, T.; Goodman, D. W. *J. Phys. Chem. B* **2005**, *109*, 18535.
- (43) Park, J. B.; Ratliff, J. S.; Ma, S.; Chen, D. A. *J. Phys. Chem. C* **2007**, *111*, 2165.
- (44) Benten, W.; Nilius, N.; Ernst, N.; Freund, H. J. *Phys. Rev. B* **2005**, *72*, 045403.
- (45) Roldan Cuena, B.; Baek, S. H.; Jaramillo, T. F.; McFarland, E. W. *J. Am. Chem. Soc.* **2003**, *125*, 12928.
- (46) Diebold, U. *Surf. Sci. Rep.* **2003**, *48*, 53.
- (47) Chusuei, C. C.; Lai, X.; Luo, K.; Goodman, D. W. *Top. Catal.* **2001**, *14*, 71.
- (48) Wagner, C. D.; Naumkin, A. V.; Kraut-Vass, A.; Allison, J. W.; Powell, C. J.; Rumble, J. R., Jr. X-ray Photoelectron Spectroscopy Database, Version 3.5 (Web version, <http://srdata.nist.gov/xps>), National Institute of Standards and Technology (NIST).
- (49) Pinault, M.; Mayne-L'Hermitte, M.; Reynaud, C.; Pichot, V.; Launois, P.; Balltaud, D. *Carbon* **2005**, *43*, 2968.
- (50) Mathieu, H. J.; Landolt, D. *Corros. Sci.* **1986**, *26*, 547.
- (51) Pan, J. M.; Madey, T. E. *J. Vac. Sci. Technol. A* **1993**, *11*, 1667.
- (52) Fujii, T.; Takada, Y.; Nakanishi, M.; Takada, J.; Kimura, M.; Yoshikawa, H. *J. Phys.: Conf. Series* **2008**, *100*, 012043.
- (53) Onishi, H.; Iwasawa, Y. *Phys. Rev. Lett.* **1996**, *76*, 791.
- (54) Tanner, R. E.; Castell, M. R.; Briggs, G. A. D. *Surf. Sci.* **1998**, *413*, 672.
- (55) Chen, M. S.; Goodman, D. W. *Acc. Chem. Res.* **2006**, *39*, 739.
- (56) Stone, P.; Bennett, R. A.; Bowker, M. *New J. Phys.* **1999**, *1*, 1.
- (57) Pireaux, J. J.; Liehr, M.; Thiry, P. A.; Delrue, J. P.; Caudano, R. *Surf. Sci.* **1984**, *141*, 221.
- (58) Irissou, E.; Denis, M. C.; Chaker, M.; Guay, D. *Thin Solid Films* **2005**, *472*, 49.
- (59) Boyen, H. G.; Kastle, G.; Weigl, F.; Koslowski, B.; Dietrich, C.; Zieman, P.; Spatz, J. P.; Riethmuller, S.; Hartmann, C.; Moller, M.; Schmid, G.; Garnier, M. G.; Oelhafen, P. *Science* **2002**, *297*, 1533.
- (60) Lim, D. C.; Lopez-Salido, I.; Dietsche, R.; Bubek, M.; Kim, Y. D. *Surf. Sci.* **2006**, *600*, 507.
- (61) Koslowski, B.; Boyen, H. G.; Wilderotter, C.; Kastle, G.; Zieman, P.; Wahnenberg, R.; Oelhafen, P. *Surf. Sci.* **2001**, *475*, 1.
- (62) Tsai, H. C.; Hu, E.; Perng, K.; Chen, M. K.; Wu, J. C.; Chang, Y. S. *Surf. Sci.* **2003**, *537*, L447.
- (63) Ono, L. K.; Roldan Cuena, B. *J. Phys. Chem. C* **2008**, *112*, 4676.
- (64) Wertheim, G. K.; Dicenzo, S. B.; Youngquist, S. E. *Phys. Rev. Lett.* **1983**, *51*, 2310.
- (65) Howard, A.; Clark, D. N. S.; Mitchell, C. E. J.; Egglestine, R. G.; Danaher, V. R. *Surf. Sci.* **2002**, *518*, 210.
- (66) Diebold, U.; Pan, J. M.; Madey, T. E. *Surf. Sci.* **1995**, *331*–333, 845.
- (67) Deng, J.; Wang, D.; Wei, X.; Zhai, R.; Wang, H. *Surf. Sci.* **1991**, *249*, 213.
- (68) Pana, O.; Teodorescu, C. M.; Chauvet, O.; Payen, C.; Macovei, D.; Turcu, R.; Soran, M. L.; Aldea, N.; Barbu, L. *Surf. Sci.* **2007**, *601*, 4352.
- (69) Mirdamadi-Esfahani, M.; Mostafavi, M.; Keita, B.; Nadjo, L.; Kooyman, P.; Etcheberry, A.; Imperio, M.; Remita, H. *Gold Bull.* **2008**, *41*, 98.
- (70) Bischoff, M. M. J.; Yamada, T.; Quinn, A. J.; van der Kraan, R. G. P.; van Kempen, H. *Phys. Rev. Lett.* **2001**, *8724*, 246102.
- (71) Pastor, C. J.; Limones, C.; Hinarejos, J. J.; Garcia, J. M.; Miranda, R.; Gomez-Goni, J.; Ortega, J. E.; Abruna, H. D. *Surf. Sci.* **1996**, *364*, L505.
- (72) Vystavel, T.; Palasantzas, G.; Koch, S. A.; De Hosson, J. T. M. *Appl. Phys. Lett.* **2003**, *82*, 197.
- (73) Wang, Y. H.; Lin, J.; Huan, C. H. A.; Chen, G. S. *Appl. Phys. Lett.* **2001**, *79*, 680.
- (74) Ethirajan, A.; Wiedwald, U.; Boyen, H. G.; Kern, B.; Han, L. Y.; Klimmer, A.; Weigl, F.; Kastle, G.; Zieman, P.; Fauth, K.; Cai, J.; Behm, R. J.; Romanyuk, A.; Oelhafen, P.; Walther, P.; Biskupek, J.; Kaiser, U. *Adv. Mater.* **2007**, *19*, 406.
- (75) Boyen, H. G.; Kastle, G.; Zurn, K.; Herzog, T.; Weigl, F.; Zieman, P.; Mayer, O.; Jerome, C.; Moller, M.; Spatz, J. P.; Garnier, M. G.; Oelhafen, P. *Adv. Funct. Mater.* **2003**, *13*, 359.
- (76) Herzing, A. A.; Kiely, C. J.; Carley, A. F.; Landon, P.; Hutchings, G. J. *Science* **2008**, *321*, 1331.
- (77) Matthey, D.; Wang, J. G.; Wendt, S.; Matthiesen, J.; Schaub, R.; Laegsgaard, E.; Hammer, B.; Besenbacher, F. *Science* **2007**, *315*, 1692.
- (78) See, A. K.; Bartynski, R. A. *Phys. Rev. B* **1994**, *50*, 12064.
- (79) Dulub, O.; Hebenstreit, W.; Diebold, U. *Phys. Rev. Lett.* **2000**, *84*, 3646.

- (80) Croy, J. R.; Mostafa, S.; Hickman, L.; Heinrich, H.; Roldan Cuenya, B. *Appl. Catal., A* **2008**, *350*, 207.
- (81) Massalski, T. B. *Binary Alloy Phase Diagrams*; Okamoto, H., Subramanian, P. R., Kacprzak, L., Eds.; ASM International: Materials Park, OH, 1992; Vol. 1.
- (82) Skriver, H. L.; Rosengaard, N. M. *Phys. Rev. B* **1992**, *46*, 7157.
- (83) Zhang, L.; Persaud, R.; Madey, T. E. *Phys. Rev. B* **1997**, *56*, 10549.
- (84) Chen, M. S.; Luo, K.; Kumar, D.; Wallace, W. T.; Yi, C. W.; Gath, K. K.; Goodman, D. W. *Surf. Sci.* **2007**, *601*, 632.
- (85) Huber, K. P.; Herzberg, G. *Constants of Diatomic Molecules*; Van Nostrand Reinhold: New York, 1979.
- (86) Belbruno, J. J. *Heteroatom Chem.* **1998**, *9*, 651.
- (87) Lian, L.; Su, C. X.; Armentrout, P. B. *J. Chem. Phys.* **1992**, *97*, 4072.
- (88) Irigoras, A.; Michelini, M. C.; Sicilia, E.; Russo, N.; Mercero, J. M.; Ugalde, J. M. *Chem. Phys. Lett.* **2003**, *376*, 310.
- (89) Gingerich, K. A. In *Current Topics in Materials Science*; Kaldus, E., Ed.; North-Holland: Amsterdam, 1980; Vol. 6, p 345.
- (90) Wu, Z. *J. Chem. Phys. Lett.* **2005**, *406*, 24.
- (91) Goodman, D. W. *J. Catal.* **2003**, *216*, 213.
- (92) Gong, X. Q.; Selloni, A.; Dulub, O.; Jacobson, P.; Diebold, U. *J. Am. Chem. Soc.* **2008**, *130*, 370.
- (93) Iddir, H.; Ogut, S.; Browning, N. D.; Disko, M. M. *Phys. Rev. B* **2006**, *73*, 039902.
- (94) Iddir, H.; Ogut, S.; Browning, N. D.; Disko, M. M. *Phys. Rev. B* **2005**, *72*, 081407.
- (95) Gutsev, G. L.; Mochena, M. D.; Jena, P.; Bauschlicher, C. W.; Partridge, H. *J. Chem. Phys.* **2004**, *121*, 6785.
- (96) Hettich, R. L.; Freiser, B. S. *J. Am. Chem. Soc.* **1987**, *109*, 3537.
- (97) Pan, J. M.; Madey, T. E. *Catal. Lett.* **1993**, *20*, 269.

JP806570A